

On the implementation of an adaptive multirate framework for coupled transport and flow

Marius Paul Bruchhäuser^{*} · Uwe Köcher[†] · Markus Bause[‡]

Helmut Schmidt University, University of the Federal Armed Forces Hamburg, Faculty of Mechanical Engineering, Chair of Numerical Mathematics
Holstenhofweg 85, 22043 Hamburg, Germany

Abstract

In this work, a multirate in time approach resolving the different time scales of a convection-dominated transport and coupled fluid flow is developed and studied in view of goal-oriented error control by means of the Dual Weighted Residual (DWR) method. Key ingredients are an arbitrary degree discontinuous Galerkin time discretization of the underlying subproblems, an a posteriori error representation for the transport problem coupled with flow and its implementation using space-time tensor-product spaces. The error representation allows the separation of the temporal and spatial discretization error which serve as local error indicators for adaptive mesh refinement. The performance of the approach and its software implementation are studied by numerical convergence examples as well as an example of physical interest for convection-dominated transport.

Keywords: Multirate in Time · Coupled Problems · Space-Time Adaptivity · Goal-Oriented A Posteriori Error Control · Dual Weighted Residual Method

1 Introduction

In recent years, mathematical models of multi-physics coupling subproblems with characteristic time scales that differ by orders of magnitude have attracted researchers' interest; cf., e.g., [1, 2, 3, 4]. Their efficient numerical simulation with regard to the temporal discretization does not become feasible without using techniques adapted to these characteristic scales that resolve the solution components on their respective time length by an adaptation of the time steps sizes. Such methods are referred to as multirate in time (for short, multirate) schemes. Firstly, they were introduced for the numerical approximation of systems of ordinary differential equations in [5, 6]. For a short review of multirate methods including a list of references we refer to [3, 7].

In this work we focus on the multirate implementation of a fully space-time adaptive convection-dominated transport problem coupled with a time-dependent Stokes flow problem. The implementation is based on our open-source code given by [8] for the `deal.II` finite element analysis library; cf. [9]. With regard to our coupled model problem, we assume a highly time-dynamic process modeled by the transport equation such that the underlying temporal mesh is discretized using smaller time step sizes compared to a slowly moving

^{*}bruchhaeuser@hsu-hamburg.de (*corresponding author)

[†]koecher@hsu-hamburg.de

[‡]bause@hsu-hamburg.de

process modeled by the viscous flow problem. Our motivation comes through the definition of so-called characteristic times for the two subproblems that serve as quantities to measure the underlying dynamic in time and have their origin in the field of natural sciences and engineering sciences, cf., e.g., [10, 11]. For the sake of physical realism, the transport problem is supposed to be convection-dominated by assuming high Péclet numbers that are characterized by small diffusion relative to the convection, cf. [12, 13]. The solution of these transport problems are typically characterized by the occurrence of sharp moving fronts and layers. The key challenge for the numerical approximation exists in the accurate and efficient solution while avoiding non-physical oscillations or smearing effects. The application of stabilization techniques is a typical approach to overcome non-physical effects. As shown in a comparative study for time-dependent convection-diffusion-reaction equations in [14], stabilization techniques on globally refined meshes fail to avoid these oscillations even after tuning stabilization parameters. For a general review of stabilization techniques we refer to [15, 13].

For the efficient numerical simulation of multi-physics problems handling the challenges described above, it is indisputable that adaptive mesh refinement strategies in space and time are necessary. One possible technique for those adaptive strategies is goal-oriented a posteriori error control based on the Dual Weighted Residual method [16, 17]. For a general review of a posteriori error estimation we refer to [18, 19].

In this work we follow our approaches and implementations from [20, 8]. An extension to our preceding work is that the flow problem now depends on time and needs to be solved on a different time scale than the transport problem. Precisely, this work is characterised by the following features.

- Development of a multirate concept with independent time scales for the transport and flow problem, respectively.
- Implementation of tensor-product space-time slabs for an arbitrary order discontinuous Galerkin (dG) time discretization.
- Implementation of coupling the Stokes flow velocity to the transport problem using interpolation techniques between different finite element spaces and meshes.

This work is organized as follows. In Sec. 2 we introduce the model problem, the multirate decoupling of the transport and flow problems and their space-time discretizations. In Sec. 3 we derive an a posteriori error representation for the transport problem. In Sec. 4 we explain the implementation of the space-time tensor-product spaces. The underlying algorithm and some related aspects are presented in Sec. 5. Numerical examples are given in Sec. 6 and in Sec. 7 we summarize with conclusions and give some outlook for future work.

2 Model Problem, Multirate and Space-Time Discretization

In Subsection 2.1 we introduce the model problem of a convection-diffusion-reaction transport coupled with a time-dependent Stokes flow. For instance, such system is used to model species or heat transport in a creeping viscous fluid. Beyond that, such multi-physics systems of coupled flow and transport serve as prototype models for applications in several branches of natural and engineering sciences, for instance, contaminant transport and degradation in the subsurface, reservoir simulation, fluid-structure interaction, and thermal and mass transport in deformable porous media or thermal expansion in solid mechanics; cf., e.g., [21, 22, 23, 24, 25].

In Section 2.2, we explain our multirate in time approach for the two subproblems, before we present the details of the space-time discretizations in Sections 2.3-2.5.

2.1 Model Problem

The time dependent convection-diffusion-reaction transport problem in dimensionless form is given by

$$\begin{aligned} \partial_t u - \nabla \cdot (\varepsilon \nabla u) + \mathbf{v} \cdot \nabla u + \alpha u &= g \quad \text{in } Q = \Omega \times I, \\ u &= u_D \quad \text{on } \Sigma_D = \Gamma_D \times I, \\ \varepsilon \nabla u \cdot \mathbf{n} &= u_N \quad \text{on } \Sigma_N = \Gamma_N \times I, \\ u &= u_0 \quad \text{on } \Sigma_0 = \Omega \times \{0\}, \end{aligned} \quad (2.1)$$

for a boundary partition $\partial\Omega = \Gamma_D \cup \Gamma_N$, $\Gamma_D \neq \emptyset$ with outer unit normal vector \mathbf{n} . The characteristic time $t_{\text{transport}}$ of this transport equation (2.1) can be comprehended as a dimensionless time variable depending on the diffusive, convective as well as reactive part and is here defined by

$$t_{\text{transport}} := \min \left\{ \frac{L^2}{\varepsilon}; \frac{L}{V}; \frac{1}{\alpha} \right\}, \quad (2.2)$$

where $0 < \varepsilon \ll 1$ is the diffusion coefficient, $\alpha > 0$ is the reaction coefficient, L denotes the characteristic length of the domain Ω , for instance, its diameter, and V denotes a characteristic velocity of the flow field \mathbf{v} , for instance, the mean inflow velocity given by $\frac{1}{T|\Gamma_{\text{inflow}}|} \int_I \int_{\Gamma_{\text{inflow}}} \mathbf{v}_D \cdot (-\mathbf{n}) \, d\sigma \, dt$; cf. [10, 11] for more details.

The convection field \mathbf{v} in the transport problem (2.1) is determined by the dimensionless Stokes flow system

$$\begin{aligned} \partial_t \mathbf{v} - \nabla \cdot (2\nu \boldsymbol{\epsilon}(\mathbf{v}) + p\mathbf{I}) &= \mathbf{f} \quad \text{in } Q = \Omega \times I, \\ \nabla \cdot \mathbf{v} &= 0 \quad \text{in } Q = \Omega \times I, \\ \mathbf{v} &= \mathbf{v}_D \quad \text{on } \Sigma_{\text{inflow}} = \Gamma_{\text{inflow}} \times I, \\ \mathbf{v} &= \mathbf{0} \quad \text{on } \Sigma_{\text{wall}} = \Gamma_{\text{wall}} \times I, \\ (2\nu \boldsymbol{\epsilon}(\mathbf{v}) + p\mathbf{I})\mathbf{n} &= \mathbf{0} \quad \text{on } \Sigma_{\text{outflow}} = \Gamma_{\text{outflow}} \times I, \\ \mathbf{v} &= \mathbf{v}_0 \quad \text{on } \Sigma_0 = \Omega \times \{0\}, \end{aligned} \quad (2.3)$$

for a boundary partition $\partial\Omega = \Gamma_{\text{inflow}} \cup \Gamma_{\text{wall}} \cup \Gamma_{\text{outflow}}$ which is (in general) independent from the boundary partition of the transport problem. The appropriate choice for the boundary partition and setting of the inflow profiles is standard and can be found in the literature [26]. The characteristic time t_{flow} of the Stokes flow equation is then defined by

$$t_{\text{flow}} := \frac{L}{V}, \quad (2.4)$$

with L and V being chosen as in (2.2). With regard to the characteristic times of the two subproblems, we assume that $t_{\text{transport}} \ll t_{\text{flow}}$ such that we are using a finer temporal mesh to resolve the dynamics of a faster process given by the transport equation compared to the slower process of the viscous, creeping flow. This multirate in time approach is described in detail in the following section.

In (2.1), (2.3), we denote by $\Omega \subset \mathbb{R}^d$, with $d = 2, 3$, a polygonal or polyhedral bounded domain with Lipschitz boundary $\partial\Omega$ and $I = (0, T]$, $0 < T < \infty$, is a finite time interval. We assume that $\nu > 0$ is a viscosity coefficient. Well-posedness of (2.1), (2.3) and the existence of a sufficiently regular solution, such that all of the arguments and terms used below are well-defined, are tacitly assumed without mentioning explicitly all technical assumptions about the data and coefficients, cf. [15] and [27].

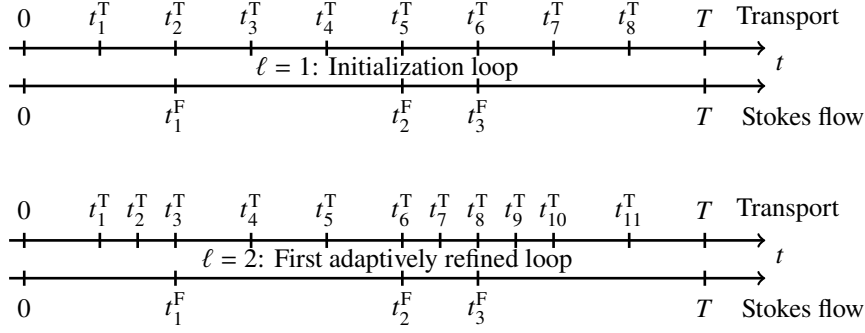


Figure 2.1: Illustration of exemplary temporal meshes for the initial loop and the first adaptively refined loop. The temporal mesh of the transport solver is adaptively refined and the mesh of the Stokes flow solver is fixed as explained in Sec. 2.2.

2.2 Multirate

For the efficient approximation we use a multirate in time approach to mimic the behaviour of a slowly moving fluid, that is approximated by a time-dependent Stokes solver, and a faster convection-diffusion-reaction process. Precisely, the problems given by (2.1) and (2.3) are considered on different time scales modeling the underlying physical processes. We initialize the temporal mesh independently for the Stokes flow and the transport problem with the following properties

- the Stokes flow temporal mesh is coarser or equal to that of the transport problem,
- the endpoints in the temporal mesh of the Stokes solver must match with endpoints in the temporal mesh of the transport problem.

We allow for adaptive time refinements of the temporal mesh of the transport problem and for global temporal mesh refinements of the Stokes solver over the adaptation loops due to the lack of an error estimator for the flow problem. An exemplary initialization and one manufactured refined temporal mesh are illustrated in Fig. 2.1.

For the multirate decoupling of the transport problem, we let $0 =: t_0^T < t_1^T < \dots < t_{N^\ell}^T := T$ a set of time points for the partition of the closure of the time domain $\bar{I} = [0, T]$ into left-open subintervals $I_n := (t_{n-1}^T, t_n^T]$, $n = 1, \dots, N^\ell$. The number N^ℓ depends on the adaptivity loop ℓ . For the flow problem, we let $0 =: t_0^F < t_1^F < \dots < t_{N^{F,\ell}}^F := T$ a set of time points for the partition of the closure of the time domain $\bar{I} = [0, T]$ into left-open subintervals $I_n^F := (t_{n-1}^F, t_n^F]$, $n = 1, \dots, N^{F,\ell}$. We approximate the solution $\{v, p\}$ of the Stokes flow problem on each I_n^F by means of a globally piecewise constant discontinuous Galerkin (dG(0)) time approximation. For simplicity of the implementation, we ensure that each element of the set $\{t_0^F, t_1^F, \dots, t_{N^{F,\ell}}^F\}$ corresponds to an element of the set $\{t_0^T, t_1^T, \dots, t_{N^\ell}^T\}$.

Additionally, we approximate the solution of the transport problem with an arbitrary degree $r \geq 0$ in time while we restrict the implementation here for the time-dependent Stokes flow to a piecewise constant in time approximation. This gives us for $r > 0$ an additional level of the multirate in time character between the two problems.

2.3 Weak Formulation

In this section, we present the weak formulation of the transport and Stokes flow problem given by Eq. (2.1) and Eq. (2.3), respectively, to prepare the discretizations in space and time following below. Let $X := \{u \in L^2(0, T; H_0^1(\Omega)) \mid \partial_t u \in L^2(0, T; H^{-1}(\Omega))\}$ and

$Y_1 := \{v \in L^2(0, T; H_0^1(\Omega)^d) \mid \partial_t v \in L^2(0, T; H^{-1}(\Omega)^d)\}$. Then, the weak formulation of (2.1) reads as follows:

For a given $v \in Y_1$ of (2.6), find $u \in X$ such that

$$A(u; v)(\varphi) = G(\varphi) \quad \forall \varphi \in X, \quad (2.5)$$

where the bilinear form $A : \{X; Y_1\} \times X \rightarrow \mathbb{R}$ and the linear form $G : L^2(0, T; H^{-1}(\Omega)) \rightarrow \mathbb{R}$ are defined by

$$\begin{aligned} A(u; v)(\varphi) &:= \int_I \{(\partial_t u, \varphi) + a(u; v)(\varphi)\} dt + (u(0), \varphi(0)), \\ G(\varphi) &:= \int_I (g, \varphi) dt + (u_0, \varphi(0)), \end{aligned}$$

with the bilinear form

$$a(u; v)(\varphi) := (\varepsilon \nabla u, \nabla \varphi) + (v \cdot \nabla u, \varphi) + (\alpha u, \varphi).$$

Here, (\cdot, \cdot) denotes the inner product of $L^2(\Omega)$ or duality pairing of $H^{-1}(\Omega)$ with $H_0^1(\Omega)$, respectively. By $\|\cdot\|$ we denote the associated L^2 -norm.

For the weak formulation of (2.3) we additionally define $Y_2 := \{p \in L^2(0, T; L_0^2(\Omega))\}$, with $L_0^2(\Omega) := \{p \in L^2(\Omega) \mid \int_\Omega p \, dx = 0\}$. Then we get:

For $f \in L^2(I; H^{-1}(\Omega)^d)$ and $v_0 \in L^2(\Omega)^d$, find $\{v, p\} \in Y_1 \times Y_2$, such that

$$B(v, p)(\psi, \chi) = F(\psi) \quad \forall \{\psi, \chi\} \in Y_1 \times Y_2, \quad (2.6)$$

where the bilinear form $B : \{Y_1 \times Y_2\} \times \{Y_1 \times Y_2\} \rightarrow \mathbb{R}$ as well as the linear form $F : L^2(0, T; H^{-1}(\Omega)^d) \rightarrow \mathbb{R}$ are defined by

$$\begin{aligned} B(v, p)(\psi, \chi) &:= \int_I \{(\partial_t v, \psi) + (2v \varepsilon(v), \varepsilon(\psi)) - (p, \nabla \cdot \psi) - (\nabla \cdot v, \chi)\} dt \\ &\quad + (v(0), \psi(0)), \\ F(\psi) &:= \int_I \{(f, \psi)\} dt + (v_0, \psi(0)). \end{aligned}$$

2.4 Discretization in Time

The sets of time subintervals I_n and I_n^F as introduced in Sec. 2.2 are finite and countable. Therefore, the separation of the global space-time cylinder $Q = \Omega \times I$ into a partition of space-time slabs $\hat{Q}_n = \Omega \times I_n$ for the transport problem and $\hat{Q}_n^F = \Omega \times I_n^F$ for the Stokes flow problem, respectively, is reasonable. The time domain of each space-time slab \hat{Q}_n or \hat{Q}_n^F is then discretized using a one-dimensional triangulation $\mathcal{T}_{\tau, n}$ or $\mathcal{T}_{\sigma, n}$ for the closure of the subinterval $\bar{I}_n = [t_{n-1}^T, t_n^T]$ or $\bar{I}_n^F = [t_{n-1}^F, t_n^F]$, respectively. This allows to have more than one cell in time on a slab \hat{Q}_n or \hat{Q}_n^F and a different number of cells in time of pairwise different slabs \hat{Q}_i and \hat{Q}_j or \hat{Q}_i^F and \hat{Q}_j^F , $0 < i, j \leq N^\ell, N^{F, \ell}$, for the ℓ -th adaptivity loop. Furthermore, let \mathcal{F}_τ and \mathcal{F}_σ be the sets of all interior time points given as

$$\begin{aligned} \mathcal{F}_\tau &:= (\{t_1^T, \dots, t_{N^\ell}^T\} \cup \{t \in \partial K_n \mid K_n \in \mathcal{T}_{\tau, n}\}) \setminus \{0, T\} \\ \mathcal{F}_\sigma &:= (\{t_1^F, \dots, t_{N^{F, \ell}}^F\} \cup \{t \in \partial K_n \mid K_n \in \mathcal{T}_{\sigma, n}\}) \setminus \{0, T\} \end{aligned}$$

with $1 \leq n \leq N^\ell, N^{F, \ell}$. The commonly used time step size τ_K or σ_K is here the diameter or length of the cell in time of $\mathcal{T}_{\tau, n}$ or $\mathcal{T}_{\sigma, n}$ and the global time discretization parameter τ

or σ is the maximum time step size τ_K or σ_K of all cells in time of all slabs \hat{Q}_n or \hat{Q}_n^F , $0 < n \leq N^\ell, N^{F,\ell}$.

For the discretization in time of the transport problem (2.5) we use a discontinuous Galerkin method dG(r) with an arbitrary polynomial degree $r \geq 0$. Let $X_\tau^{\text{dG}(r)}$ be the time-discrete function space given as

$$X_\tau^{\text{dG}(r)} := \left\{ u_\tau \in L^2(0, T; H_0^1(\Omega)) \mid u_\tau|_{K_n} \in \mathcal{P}_r(K_n; H_0^1(\Omega)), \right. \\ \left. K_n \in \mathcal{T}_{\tau,n}, n = 1, \dots, N^\ell, u_\tau(0) \in L^2(\Omega) \right\}, \quad (2.7)$$

where $\mathcal{P}_r(K_n; H_0^1(\Omega))$ denotes the space of all polynomials in time up to degree $r \geq 0$ on $K_n \in \mathcal{T}_{\tau,n}$ with values in $H_0^1(\Omega)$. For some discontinuous in time function $u_\tau \in X_\tau^{\text{dG}(r)}$ we define the limits $u_\tau(t_F^\pm)$ from above and below of u_τ at t_F as well as their jump at t_F by

$$u_\tau(t_F^\pm) := \lim_{t \rightarrow t_F^\pm} u_\tau(t), \quad [u_\tau]_{t_F} := u_\tau(t_F^+) - u_\tau(t_F^-).$$

The semidiscretization in time of the the transport problem (2.5) then reads as follows:
For a given $\mathbf{v}_\sigma \in Y_\sigma^{\text{dG}(r)}$ of (2.12), find $u_\tau \in X_\tau^{\text{dG}(r)}$ such that

$$A_\tau(u_\tau; \mathbf{v})(\varphi_\tau) = G_\tau(\varphi_\tau) \quad \forall \varphi_\tau \in X_\tau^{\text{dG}(r)}, \quad (2.8)$$

where the semi-discrete bilinear form and linear form are given by

$$A_\tau(u_\tau; \mathbf{v})(\varphi_\tau) := \sum_{n=1}^{N^\ell} \sum_{K_n \in \mathcal{T}_{\tau,n}} \int_{K_n} \{(\partial_t u_\tau, \varphi_\tau) + a(u_\tau; \mathbf{v}_\sigma)(\varphi_\tau)\} dt \\ + (u_\tau(0^+), \varphi_\tau(0^+)) + \sum_{t_F \in \mathcal{F}_\tau} ([u_\tau]_{t_F}, \varphi_\tau(t_F^+)), \quad (2.9)$$

$$G_\tau(\varphi_\tau) := \int_I (g, \varphi_\tau) dt + (u_0, \varphi_\tau(0^+)),$$

with the bilinear form $a(\cdot, \cdot)(\cdot)$ depending on the semi-discrete Stokes solution \mathbf{v}_σ .

Remark 2.1 For the error $e = u - u_\tau$ we get by subtracting Eq. (2.8) from Eq. (2.5) the identity

$$\sum_{n=1}^{N^\ell} \sum_{K_n \in \mathcal{T}_{\tau,n}} \int_{K_n} \{(\partial_t e, \varphi_\tau) + a(e, \mathbf{v}_\sigma)(\varphi_\tau)\} dt \\ + \sum_{t_F \in \mathcal{F}_\tau} ([e]_{t_F}, \varphi_\tau(t_F^+)) + (e(0^+), \varphi_\tau(0^+)) \\ = - \sum_{n=1}^{N^\ell} \sum_{K_n \in \mathcal{T}_{\tau,n}} \int_{K_n} ((\mathbf{v} - \mathbf{v}_\sigma) \cdot \nabla u, \varphi_\tau) dt, \quad (2.10)$$

with a non-vanishing right-hand side term depending on the stabilization and the error in the approximation of the flow field. Eq. (2.10) with the perturbation term on the right-hand side replaces the standard Galerkin orthogonality of the space-time finite element approximation.

The discontinuous time-discrete function space for the Stokes flow problem is given by

$$Y_\sigma^{\text{dG}(r)} := \left\{ \{\mathbf{v}_\sigma, p_\sigma\} \in L^2(0, T; H_0^1(\Omega)^d \times L_0^2(\Omega)) \mid \right. \\ \left. \mathbf{v}_\sigma|_{K_n} \in \mathcal{P}_r(K_n; H_0^1(\Omega)^d), \mathbf{v}_\sigma(0) \in L^2(\Omega), \right. \\ \left. p_\sigma|_{K_n} \in \mathcal{P}_r(K_n; L_0^2(\Omega)), K_n \in \mathcal{T}_{\sigma,n}, n = 1, \dots, N^{F,\ell} \right\}. \quad (2.11)$$

Then, the semidiscretization in time of the the Stokes flow problem (2.6) reads as follows:

Find $\{\mathbf{v}_\sigma, p_\sigma\} \in Y_\sigma^{\text{dG}(r)}$ such that

$$B_\sigma(\mathbf{v}_\sigma, p_\sigma)(\boldsymbol{\psi}_\sigma, \chi_\sigma) = F_\sigma(\boldsymbol{\psi}_\sigma) \quad \forall \{\boldsymbol{\psi}_\sigma, \chi_\sigma\} \in Y_\sigma^{\text{dG}(r)}, \quad (2.12)$$

where the semi-discrete bilinear form and linear form are given by

$$\begin{aligned} B_\sigma(\mathbf{v}_\sigma, p_\sigma)(\boldsymbol{\psi}_\sigma, \chi_\sigma) &:= \sum_{n=1}^{N^{\text{F}, \ell}} \sum_{K_n \in \mathcal{T}_{\sigma, n}} \int_{K_n} \{(\partial_t \mathbf{v}_\sigma, \boldsymbol{\psi}_\sigma) + (2\nu \boldsymbol{\epsilon}(\mathbf{v}_\sigma), \boldsymbol{\epsilon}(\boldsymbol{\psi}_\sigma)) \\ &\quad - (p_\sigma, \nabla \cdot \boldsymbol{\psi}_\sigma) - (\nabla \cdot \mathbf{v}_\sigma, \chi_\sigma)\} dt \\ &\quad + (\mathbf{v}_\sigma(0^+), \boldsymbol{\psi}_\sigma(0^+)) + \sum_{t_F \in \mathcal{F}_\sigma} ([\mathbf{v}_\sigma]_{t_F}, \boldsymbol{\psi}_\sigma(t_F^+)), \\ F_\sigma(\varphi_\tau) &:= \int_I (f, \boldsymbol{\psi}_\sigma) dt + (\mathbf{v}_0, \boldsymbol{\psi}_\sigma(0^+)). \end{aligned} \quad (2.13)$$

2.5 Discretization in Space and SUPG Stabilization

Next, we describe the Galerkin finite element approximation in space of the semi-discrete transport problem (2.8) and the flow problem (2.12), respectively. We use Lagrange type finite element spaces of continuous functions that are piecewise polynomials. For the discretization in space, we consider a separation $\mathcal{Q}_n = \mathcal{T}_{h, n} \times I_n$ or $\mathcal{Q}_n^{\text{F}} = \mathcal{T}_{h, n}^{\text{F}} \times I_n^{\text{F}}$, where $\mathcal{T}_{h, n}$ or $\mathcal{T}_{h, n}^{\text{F}}$ build a decomposition of the domain Ω into disjoint elements K or K^{F} , such that $\overline{\Omega} = \cup_{K \in \mathcal{T}_h} \overline{K}$ or $\overline{\Omega} = \cup_{K^{\text{F}} \in \mathcal{T}_h^{\text{F}}} \overline{K^{\text{F}}}$ for the transport and Stokes flow problem, respectively. Here, we choose the elements $K \in \mathcal{T}_h$ or $K^{\text{F}} \in \mathcal{T}_h^{\text{F}}$ to be quadrilaterals for $d = 2$ and hexahedrals for $d = 3$. We denote by h_K or h_K^{F} the diameter of the element K or K^{F} . The global space discretization parameter h or h^{F} is given by $h := \max_{K \in \mathcal{T}_h} h_K$ or $h^{\text{F}} := \max_{K^{\text{F}} \in \mathcal{T}_h^{\text{F}}} h_K^{\text{F}}$, respectively. Our mesh adaptation process yields locally refined cells, which is enabled by using hanging nodes. We point out that the global conformity of the finite element approach is preserved since the unknowns at such hanging nodes are eliminated by interpolation between the neighboring 'regular' nodes; cf. [17, Chapter 4.2] and [28] for more details. On \mathcal{T}_h and \mathcal{T}_h^{F} we define the discrete finite element spaces by $V_h^{p, n} := \{v \in C(\overline{\Omega}) \mid v|_K \in \mathcal{Q}_h^p(K), \forall K \in \mathcal{T}_h\}$, and $V_{h^{\text{F}}}^{p, n} := \{v \in C(\overline{\Omega}) \mid v|_{K^{\text{F}}} \in \mathcal{Q}_h^p(K^{\text{F}}), \forall K^{\text{F}} \in \mathcal{T}_h^{\text{F}}\}$, with $1 \leq n \leq N, N^{\text{F}}$, where $\mathcal{Q}_h^p(K)$ or $\mathcal{Q}_{h^{\text{F}}}^p(K^{\text{F}})$ is the space defined on the reference element with maximum degree p in each variable. By replacing $H_0^1(\Omega)$ in the definition of the semi-discrete function space $X_\tau^{\text{dG}(r)}$ in (2.7) by $V_h^{p, n}$ and by replacing $H_0^1(\Omega)^d, L_0^2(\Omega)$ in the definition of the semi-discrete function space $Y_\sigma^{\text{dG}(r)}$ in (2.11) by $V_{h^{\text{F}}}^{p, n}$, we obtain the fully discrete function spaces for the transport and Stokes flow problem, respectively,

$$\begin{aligned} X_{\tau h}^{\text{dG}(r), p} &:= \left\{ \begin{aligned} &u_{\tau h} \in X_\tau^{\text{dG}(r)} \mid u_{\tau h}|_{K_n} \in \mathcal{P}_r(K_n; H_h^{p_u, n}), \\ &u_{\tau h}(0) \in H_h^{p_u, 0}, K_n \in \mathcal{T}_{\tau, n}, n = 1, \dots, N \end{aligned} \right\}, \\ Y_{\sigma h^{\text{F}}}^{\text{dG}(r), p} &:= \left\{ \begin{aligned} &\{\mathbf{v}_{\sigma h}, p_{\sigma h}\} \in Y_\sigma^{\text{dG}(r)} \mid \mathbf{v}_{\sigma h}|_{K_n} \in \mathcal{P}_r(K_n; (H_h^{p_v, n})^d), \\ &\mathbf{v}_{\sigma h}(0) \in (H_h^{p_v, 0})^d, p_{\sigma h}|_{K_n} \in \mathcal{P}_r(K_n; L_h^{p_p, n}), \\ &K_n \in \mathcal{T}_{\sigma, n}, n = 1, \dots, N^{\text{F}, \ell} \end{aligned} \right\} \end{aligned} \quad (2.14)$$

$$H_h^{p_u, n} := V_h^{p_u, n} \cap H_0^1(\Omega), \quad H_h^{p_v, n} := V_h^{p_v, n} \cap H_0^1(\Omega), \quad L_h^{p_p, n} := V_h^{p_p, n} \cap L_0^2(\Omega).$$

We note that the spatial finite element space $V_h^{p, n}$ and $V_{h^{\text{F}}}^{p, n}$ are allowed to be different on all subintervals I_n and I_n^{F} , respectively, which is natural in the context of a discontinuous Galerkin

approximation of the time variable and allows dynamic mesh changes in time. Due to the conformity of $H_h^{pu,n}$, $H_h^{pv,n}$ and $L_h^{pp,n}$, we get $X_{\tau h}^{\text{dG}(r),p} \subseteq X_\tau^{\text{dG}(r)}$ and $Y_{\sigma h^F}^{\text{dG}(r),p} \subseteq Y_\sigma^{\text{dG}(r)}$, respectively.

For convection-dominated transport, the finite element approximation needs to be stabilized in order to avoid spurious and non-physical oscillations of the discrete solution arising close to sharp fronts and layers. Here, we apply the streamline upwind Petrov-Galerkin (SUPG) method introduced by Hughes and Brooks [29, 30]. With this in mind, the stabilized fully discrete discontinuous in time scheme for the transport problem reads as follows:

For a given $\mathbf{v}_{\sigma h} \in Y_{\sigma h^F}^{\text{dG}(r),p}$ of (2.18), find $u_{\tau h} \in X_{\tau h}^{\text{dG}(r),p}$ such that

$$A_S(u_{\tau h}; \mathbf{v}_{\sigma h})(\varphi_{\tau h}) = G_\tau(\varphi_{\tau h}) \quad \forall \varphi_{\tau h} \in X_{\tau h}^{\text{dG}(r),p}, \quad (2.15)$$

where the linear form $G_\tau(\cdot)$ is defined in (2.9) and the stabilized bilinear form $A_S(\cdot; \cdot)(\cdot)$ is given by

$$A_S(u_{\tau h}; \mathbf{v}_{\sigma h})(\varphi_{\tau h}) := A_\tau(u_{\tau h}; \mathbf{v}_{\sigma h})(\varphi_{\tau h}) + S_A(u_{\tau h}; \mathbf{v}_{\sigma h})(\varphi_{\tau h}),$$

with $A_\tau(\cdot; \cdot)(\cdot)$ being defined in (2.9). Here, the SUPG stabilized bilinear form $S_A(\cdot; \cdot)(\cdot)$ is defined by

$$\begin{aligned} S_A(u_{\tau h}; \mathbf{v}_{\sigma h})(\varphi_{\tau h}) := & \sum_{n=1}^{N^\ell} \sum_{K_n \in \mathcal{T}_{\tau,n}} \int_{K_n} \sum_{K \in \mathcal{T}_h} \delta_K (r(u_{\tau h}), \mathbf{v}_{\sigma h} \cdot \nabla \varphi_{\tau h})_K \, dt \\ & + \sum_{t_F \in \mathcal{F}_\tau} \sum_{K \in \mathcal{T}_h} \delta_K ([u_{\tau h}]_{t_F}, \mathbf{v}_{\sigma h} \cdot \nabla \varphi_{\tau h}(t_F^+))_K \\ & + \sum_{K \in \mathcal{T}_h} \delta_K (u_{\tau h,0}^+ - u_0, \mathbf{v}_{\sigma h} \cdot \nabla \varphi_{\tau h,0}^+)_K, \end{aligned} \quad (2.16)$$

where δ_K is the so-called stabilization parameter and the residual term $r(\cdot; \cdot)$ is given by

$$r(u_{\tau h}) := \partial_t u_{\tau h} - \nabla \cdot (\varepsilon \nabla u_{\tau h}) + \mathbf{v}_{\sigma h} \cdot \nabla u_{\tau h} + \alpha u_{\tau h} - g.$$

We note that the bilinear form $a(\cdot; \mathbf{v}_{\sigma h})(\cdot)$ occurring in $A_S(\cdot; \cdot)(\cdot)$ reads here as

$$a(u_{\tau h}; \mathbf{v}_{\sigma h})(\varphi_{\tau h}) = (\varepsilon \nabla u_{\tau h}, \nabla \varphi_{\tau h}) + (\mathbf{v}_{\sigma h} \cdot \nabla u_{\tau h}, \varphi_{\tau h}) + (\alpha u_{\tau h}, \varphi_{\tau h})$$

for the fully discrete solutions.

Remark 2.2 The proper choice of the stabilization parameter δ_K is an important issue in the application of the SUPG approach; cf., e.g., [31, 14, 13] and the discussion therein. For time-dependent convection-diffusion-reaction problems an optimal error estimate for $\delta_K = O(h)$ is derived in [31].

Remark 2.3 For the error $e = u_\tau - u_{\tau h}$ we get by subtracting Eq. (2.15) from Eq. (2.8) the identity

$$\begin{aligned} & \sum_{n=1}^{N^\ell} \sum_{K_n \in \mathcal{T}_{\tau,n}} \int_{K_n} \{(\partial_t e, \varphi_{\tau h}) + a(e; \mathbf{v}_{\sigma h})(\varphi_{\tau h})\} \, dt \\ & + \sum_{t_F \in \mathcal{F}_\tau} ([e]_{t_F}, \varphi_{\tau h}(t_F^+) + (e(0^+), \varphi_{\tau h}(0^+)) \\ & = S_A(u_{\tau h}; \mathbf{v}_{\sigma h})(\varphi_{\tau h}) - \sum_{n=1}^{N^\ell} \sum_{K_n \in \mathcal{T}_{\tau,n}} \int_{K_n} ((\mathbf{v}_\sigma - \mathbf{v}_{\sigma h}) \cdot \nabla u_\tau, \varphi_{\tau h}) \, dt, \end{aligned} \quad (2.17)$$

with a non-vanishing right-hand side term depending on the stabilization and the error in the approximation of the flow field. Eq. (2.17) with the perturbation term on the right-hand side replaces the standard Galerkin orthogonality of the space-time finite element approximation.

Finally, the fully discrete discontinuous in time scheme for the Stokes flow problem reads as follows:

Find $\{\mathbf{v}_{\sigma h}, p_{\sigma h}\} \in Y_{\sigma h^F}^{\text{dG}(r),p}$ such that

$$B_{\sigma}(\mathbf{v}_{\sigma h}, p_{\sigma h})(\boldsymbol{\psi}_{\sigma h}, \chi_{\sigma h}) = F_{\sigma}(\boldsymbol{\psi}_{\sigma h}) \quad \forall \{\boldsymbol{\psi}_{\sigma h}, \chi_{\sigma h}\} \in Y_{\sigma h^F}^{\text{dG}(r),p}, \quad (2.18)$$

with $B_{\sigma}(\cdot, \cdot)(\cdot, \cdot)$ and $F_{\sigma}(\cdot)$ being defined in (2.13).

3 An A Posteriori Error Estimator for the Transport Problem

In this section we derive a DWR-based a posteriori error representation for the stabilized transport problem (2.15) coupled with the flow problem via the convection tensor $\mathbf{v}_{\sigma h}$ given by Eq. (2.18). Since the derivation is close to our work based on a coupling of a steady-state Stokes problem, we keep this section rather short by drawing attention only to the differences and refer to our work [20] for a detailed version of the proofs and further details.

Here, only goal quantities depending on the unknown u are studied. For applications of practical interest, physical quantities in terms of the transport quantity u are typically of higher relevance than quantities in the unknowns \mathbf{v} and p of the flow problem. In the sequel, we introduce this goal quantity with the following properties.

Assumption (Target functional J)

Let us assume $J : X \rightarrow \mathbb{R}$ to be a linear functional representing the goal quantity of physical interest. In general, this functional is given as

$$J(u) = \int_0^T J_1(u(t)) \, dt + J_2(u(T)), \quad (3.1)$$

where $J_1 \in L^2(I; H^{-1}(\Omega))$ and $J_2 \in H^{-1}(\Omega)$ are three times differentiable functionals defining the dual right-hand side and the dual initial at time $t = T$, respectively, where each of them may be zero.

Since we aim at controlling the respective errors due to the discretization in time as well as in space, we split the a posteriori error representation with respect to J into the contributions

$$J(u) - J(u_{\tau h}) = J(u) - J(u_{\tau}) + J(u_{\tau}) - J(u_{\tau h}). \quad (3.2)$$

For the respective error representations we define the Lagrangian functionals $\mathcal{L} : X \times X \rightarrow \mathbb{R}$, $\mathcal{L}_{\tau} : X_{\tau}^{\text{dG}(r)} \times X_{\tau}^{\text{dG}(r)} \rightarrow \mathbb{R}$, and $\mathcal{L}_{\tau h} : X_{\tau h}^{\text{dG}(r),p} \times X_{\tau h}^{\text{dG}(r),p} \rightarrow \mathbb{R}$ by

$$\mathcal{L}(u, z; \mathbf{v}) := J(u) + G(z) - A(u; \mathbf{v})(z), \quad (3.3a)$$

$$\mathcal{L}_{\tau}(u_{\tau}, z_{\tau}; \mathbf{v}_{\sigma}) := J(u_{\tau}) + G_{\tau}(z_{\tau}) - A_{\tau}(u_{\tau}; \mathbf{v}_{\sigma})(z_{\tau}), \quad (3.3b)$$

$$\mathcal{L}_{\tau h}(u_{\tau h}, z_{\tau h}; \mathbf{v}_{\sigma h}) := J(u_{\tau h}) + G_{\tau}(z_{\tau h}) - A_S(u_{\tau h}; \mathbf{v}_{\sigma h})(z_{\tau h}). \quad (3.3c)$$

Here, the Lagrange multipliers z , z_{τ} , and $z_{\tau h}$ are called dual variables in contrast to the primal variables u , u_{τ} , and $u_{\tau h}$; cf. [32, 16]. Considering the directional derivatives of the Lagrangian functionals, also known as Gâteaux derivatives, with respect to their first argument, i.e.

$$\mathcal{L}'_u(u, z; \mathbf{v})(\varphi) := \lim_{t \neq 0, t \rightarrow 0} t^{-1} \{ \mathcal{L}(u + t\varphi, z; \mathbf{v}) - \mathcal{L}(u, z; \mathbf{v}) \}, \quad \varphi \in X,$$

leads to the so-called dual problems: Find the continuous dual solution $z \in X$, the semi-discrete dual solution $z_\tau \in X_\tau^{\text{dG}(r)}$ and the fully discrete dual solution $z_{\tau h} \in X_{\tau h}^{\text{dG}(r),p}$, respectively, such that

$$A'(u; \mathbf{v})(\varphi, z) = J'(u)(\varphi) \quad \forall \varphi \in X, \quad (3.4a)$$

$$A'_\tau(u_\tau; \mathbf{v}_\sigma)(\varphi_\tau, z_\tau) = J'(u_\tau)(\varphi_\tau) \quad \forall \varphi_\tau \in X_\tau^{\text{dG}(r)}, \quad (3.4b)$$

$$A'_S(u_{\tau h}; \mathbf{v}_{\sigma h})(\varphi_{\tau h}, z_{\tau h}) = J'(u_{\tau h})(\varphi_{\tau h}) \quad \forall \varphi_{\tau h} \in X_{\tau h}^{\text{dG}(r),p}, \quad (3.4c)$$

where we refer to our work [20] for a detailed description of the adjoint bilinear forms A' , A'_τ , A'_S as well as the dual right hand side term J' .

Remark 3.1 We note that the directional derivatives of the Lagrangian functionals with respect to their second argument leads to the primal problems given by Eqs. (2.5), (2.8) and (2.15), respectively.

In the following Thm. 3.2 we derive error representation formulas in space and time for the transport problem depending on the residuals of the primal and dual problem as well as jump, stabilization and coupling terms due to a non vanishing Galerkin orthogonality described in Rem. 2.1 and Rem. 2.3, respectively. The primal and dual residuals based on the continuous and semi-discrete schemes are defined by means of the Gâteaux derivatives of the Lagrangian functionals in the following way:

$$\begin{aligned} \rho(u; \mathbf{v})(\varphi) &:= \mathcal{L}'_z(u, z; \mathbf{v})(\varphi) = G(\varphi) - A(u; \mathbf{v})(\varphi), \\ \rho^*(u, z; \mathbf{v})(\varphi) &:= \mathcal{L}'_u(u, z; \mathbf{v})(\varphi) = J'(u)(\varphi) - A'(u; \mathbf{v})(\varphi, z), \\ \rho_\tau(u; \mathbf{v}_\sigma)(\varphi) &:= \mathcal{L}'_{\tau, z}(u, z; \mathbf{v}_\sigma)(\varphi) = G_\tau(\varphi) - A_\tau(u; \mathbf{v}_\sigma)(\varphi), \\ \rho_\tau^*(u, z; \mathbf{v}_\sigma)(\varphi) &:= \mathcal{L}'_{\tau, u}(u, z; \mathbf{v}_\sigma)(\varphi) = J'(u)(\varphi) - A'_\tau(u; \mathbf{v}_\sigma)(\varphi, z). \end{aligned}$$

By using these residuals as well as the Galerkin orthogonality described in Rem. 2.1 and Rem. 2.3, respectively, we get the following result for the DWR-based error representation in space and time for the transport problem.

Theorem 3.2 Let $\{u, z\} \in X \times X$, $\{u_\tau, z_\tau\} \in X_\tau^{\text{dG}(r)} \times X_\tau^{\text{dG}(r)}$, and $\{u_{\tau h}, z_{\tau h}\} \in X_{\tau h}^{\text{dG}(r),p} \times X_{\tau h}^{\text{dG}(r),p}$ denote the stationary points of \mathcal{L} , \mathcal{L}_τ , and $\mathcal{L}_{\tau h}$ on the different levels of discretization, i.e.,

$$\begin{aligned} \mathcal{L}'(u, z; \mathbf{v})(\delta u, \delta z) &= 0 \quad \forall \{\delta u, \delta z\} \in X \times X, \\ \mathcal{L}'_\tau(u_\tau, z_\tau; \mathbf{v}_\sigma)(\delta u_\tau, \delta z_\tau) &= 0 \quad \forall \{\delta u_\tau, \delta z_\tau\} \in X_\tau^{\text{dG}(r)} \times X_\tau^{\text{dG}(r)}, \\ \mathcal{L}'_{\tau h}(u_{\tau h}, z_{\tau h}; \mathbf{v}_{\sigma h})(\delta u_{\tau h}, \delta z_{\tau h}) &= 0 \quad \forall \{\delta u_{\tau h}, \delta z_{\tau h}\} \in X_{\tau h}^{\text{dG}(r),p} \times X_{\tau h}^{\text{dG}(r),p}. \end{aligned}$$

Additionally, for the errors $e = u - u_\tau$ and $e = u_\tau - u_{\tau h}$ we have the Eqs. (2.10) and (2.17) of Galerkin orthogonality type. Then, for the discretization errors in space and time we get the representation formulas

$$\begin{aligned} J(u) - J(u_\tau) &= \frac{1}{2} \rho(u_\tau; \mathbf{v})(z - \tilde{z}_\tau) + \frac{1}{2} \rho^*(u_\tau, z_\tau; \mathbf{v})(u - \tilde{u}_\tau) \\ &\quad + \frac{1}{2} \mathcal{D}'_\tau(u_\tau, z_\tau)(\tilde{u}_\tau - u_\tau, \tilde{z}_\tau - z_\tau) \\ &\quad + \mathcal{D}_\tau(u_\tau, z_\tau) + \mathcal{R}_\tau, \end{aligned} \quad (3.5a)$$

$$\begin{aligned} J(u_\tau) - J(u_{\tau h}) &= \frac{1}{2} \rho(u_{\tau h}; \mathbf{v}_\sigma)(z_\tau - \tilde{z}_{\tau h}) + \frac{1}{2} \rho^*(u_{\tau h}, z_{\tau h}; \mathbf{v}_\sigma)(u_\tau - \tilde{u}_{\tau h}) \\ &\quad + \frac{1}{2} \mathcal{D}'_{\tau h}(u_{\tau h}, z_{\tau h})(\tilde{u}_{\tau h} - u_{\tau h}, \tilde{z}_{\tau h} - z_{\tau h}) \\ &\quad + \mathcal{D}_{\tau h}(u_{\tau h}, z_{\tau h}) + \mathcal{R}_h, \end{aligned} \quad (3.5b)$$

where $\mathcal{D}_\tau(\cdot, \cdot)$ and $\mathcal{D}_{\tau h}(\cdot, \cdot)$ are given by

$$\begin{aligned}\mathcal{D}_\tau(u_\tau, z_\tau) &= \sum_{t_F \in \mathcal{F}_\tau} ([u_\tau]_{t_F}, z_\tau(t_F^+)) - \sum_{n=1}^{N^\ell} \sum_{K_n \in \mathcal{T}_{\tau,n}} \int_{K_n} ((\mathbf{v} - \mathbf{v}_\sigma) \cdot \nabla u_\tau, z_\tau) \, dt, \\ \mathcal{D}_{\tau h}(\varphi, \psi) &= S_A(u_{\tau h}; \mathbf{v}_{\sigma h})(z_{\tau h}) - \sum_{n=1}^{N^\ell} \sum_{K_n \in \mathcal{T}_{\tau,n}} \int_{K_n} ((\mathbf{v}_\sigma - \mathbf{v}_{\sigma h}) \cdot \nabla u_{\tau h}, z_{\tau h}) \, dt,\end{aligned}\tag{3.6}$$

and $\mathcal{D}'_\tau(\cdot, \cdot)(\cdot, \cdot)$ and $\mathcal{D}'_{\tau h}(\cdot, \cdot)(\cdot, \cdot)$ denoting the Gâteaux derivatives with respect to the first and second argument and with $S_A(\cdot; \cdot)(\cdot)$ being defined in (2.16). Here, $\{\tilde{u}_\tau, \tilde{z}_\tau\} \in X_\tau^{\text{dG}(r)} \times X_\tau^{\text{dG}(r)}$, and $\{\tilde{u}_{\tau h}, \tilde{z}_{\tau h}\} \in X_{\tau h}^{\text{dG}(r),p} \times X_{\tau h}^{\text{dG}(r),p}$ can be chosen arbitrarily and the remainder terms \mathcal{R}_τ and \mathcal{R}_h are of higher-order with respect to the errors $u - u_\tau, z - z_\tau$ and $u_\tau - u_{\tau h}, z_\tau - z_{\tau h}$, respectively.

Remark 3.3 We note that within the temporal error representation formula (3.5a) additional terms due to the coupling occur, cf. Eq. (3.6). This is an extension of our previous results obtained in [33] and [20]. Furthermore, we indicate that the occurring differences $\mathbf{v} - \tilde{\mathbf{v}}_\tau$ and $\mathbf{v}_\tau - \tilde{\mathbf{v}}_{\tau h}$ with regard to the primal and dual variables are called temporal and spatial weights, respectively.

Proof. The technique to prove the temporal error representation formula (3.5a) is equivalent to the spatial counterpart that can be found in our work [20, Thm. 3.1] and was originally proved by Besier and Rannacher applied to the incompressible Navier-Stokes equations in [32, Thm. 5.2]. More precisely, we are using a general result given in [32, Lemma 5.1] with the following settings:

$$L = \mathcal{L}, \quad \tilde{L} = \mathcal{L}_\tau, \quad Y_1 = X \times X, \quad Y_2 = X_\tau^{\text{dG}(r)} \times X_\tau^{\text{dG}(r)}, \quad Y := Y_1 + Y_2,$$

where $\mathcal{L}, \mathcal{L}_\tau$ are the Lagrangian functional given by Eq. (3.3) and Y, Y_1 and Y_2 are function spaces defined in [32, Lemma 5.1]. \blacksquare

4 Implementation of Tensor-Product Spaces

In this section we analyse the implementation of space-time tensor-product spaces in detail. An exemplary illustration of a space-time cylinder that is distributed into space-time tensor-product slabs is given in Fig. 4.1. Precisely, we explain the details here for the scalar-valued transport equation with primal and dual finite element spaces. The implementation for the primal vector-valued Stokes flow problem is very similar with the difference that the spatial finite element has $d+1$ components for the velocity and pressure variables. We denote the number of spatial degrees of freedom by $N_{\text{DoF}}^{s,n}$ for one degree of freedom in time and the number of temporal degrees of freedom by $N_{\text{DoF}}^{t,n}$ on the n -th slab.

To implement the space-time tensor-product space, as illustrated in Fig. 4.1, we start with the usual discretization for the finite element method in space having only one degree of freedom in time in an adaptive time marching process, but here we do this for each slab. Therefore, we generate the geometrical triangulation, i.e. a spatial mesh, and colourize the boundaries. Boundary colours can mark for instance Dirichlet type boundary conditions, Neumann type boundary conditions, etc. Next, we initialize each slab by creating an independent copy of the generated spatial triangulation.

Then, for one degree of freedom in time on each slab, we distribute the spatial degrees of freedom and generate affine constraints objects. Remark that an affine constraints object may include information on handling degrees of freedom on hanging nodes or on Dirichlet type

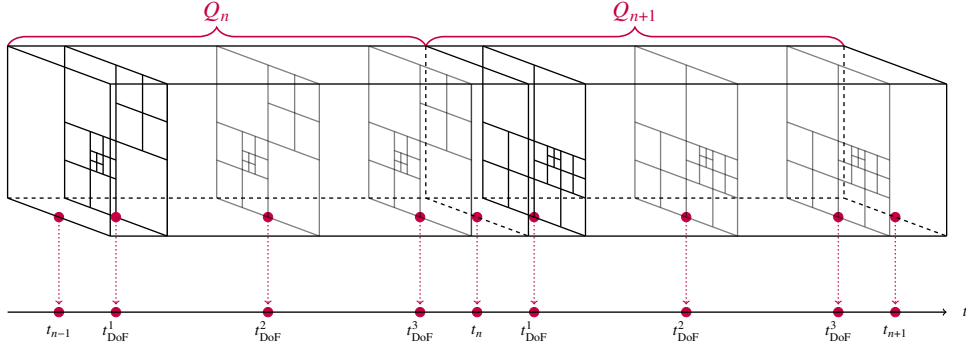


Figure 4.1: Two consecutive space-time slabs, exemplary for a discontinuous Galerkin dG(2) time discretization generated with three Gaussian quadrature points. The three degrees of freedom (DoF) time points on each slab are the support points for the temporal basis functions. Each of the illustrated slabs here has one temporal cell and an independent and adaptively refined spatial triangulation.

boundary nodes. The sparsity pattern for a sparse matrix is now generated with the geometric triangulation, the spatial degree of freedom (DoF) handler and the constraints object for one degree of freedom in time.

Next, the space-time tensor-product degrees of freedom on a slab are aligned by their local degree of freedom in time on a slab. Precisely, the first degree of freedom in time has the global number 0 and the last one has the number $N_{\text{DoF}}^{t,n} - 1$. The numbering of the local temporal degrees of freedom is increasingly ordered by their temporal mesh cell index. Remark that we have an one-dimensional additional triangulation (temporal mesh) for the time subinterval (t_{n-1}, t_n) corresponding to the n -th slab; refer to the Fig. 4.2 for details. Overall, we have $N_{\text{DoF}}^{t,n}$ times $N_{\text{DoF}}^{s,n}$ degrees of freedom on the n -th slab.

Next, the space-time tensor-product constraints are created by taking the original constraints object and shifting all entries accordingly such that the $N_{\text{DoF}}^{t,n}$ are represented. Precisely, the spatial degrees of freedom from 0 to $N_{\text{DoF}}^s - 1$ are associated to the first local temporal degree of freedom on a slab. If there are more than one temporal degrees of freedom on a slab, the corresponding spatial degrees of freedom are shifted by the number $N_{\text{DoF}}^{s,n}$ times the local temporal degree of freedom index.

For each degree of freedom in time, the sparsity pattern is now copied into the diagonal blocks for the space-time tensor product sparsity pattern. A higher-order polynomial degree in time introduces couplings between the temporal basis functions resulting in additional coupling blocks. For the case of more than one time cell per slab, additional couplings appear for temporal derivatives between the time basis functions of two consecutive time cells. For the primal problem, the evolution is forward in time and therefore these couplings appear in the left lower part. For the dual problem, the evolution is backward in time and therefore the coupling diagonals appear in the right upper part. Exemplary sparsity patterns are given in Fig. 4.3, Fig. 4.4 and Fig. 4.5.

For the assembly process we can use the basis functions and their derivatives in time similar to the classical finite element approach in space. But the distribution of the local contributions must respect the order of the temporal basis functions. First, we take the mapping from a local to a global degree of freedom in space. To respect the temporal basis functions, we shift the local to global mapping accordingly by the factor of local degrees of freedom in space on a spatial cell. This results in a shift of each global degree of freedom by the factor of $N_{\text{DoF}}^{s,n}$ times the global degree of freedom of the respective basis function in time. The local matrix has therefore the size of the local degrees of freedom on a spatial mesh cell

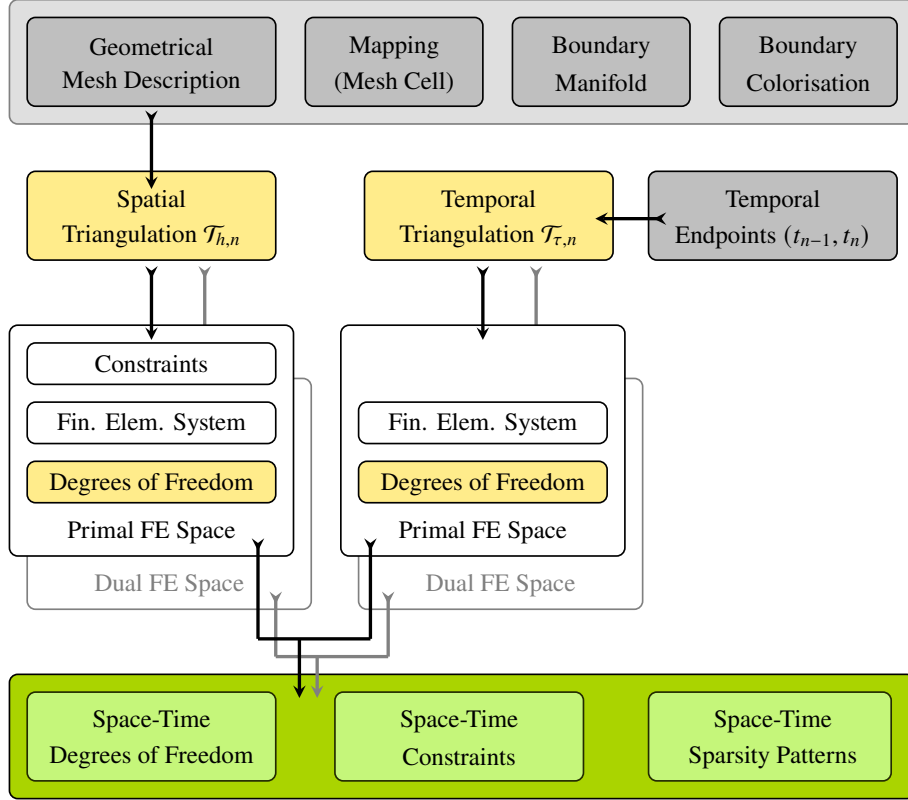


Figure 4.2: Illustration of the generation of space-time elements for tensor-product spaces on a slab.

times the local degrees of freedom in time on a temporal mesh cell.

In the case of more than one time cell per slab, an additional local matrix is assembled for the coupling of the trial basis functions of the previous time cell and the test basis functions of the current time cell. This implements the negative part of the jump trace operator in time which is transferred to the right-hand side in a classical time marching approach.

Finally, the space-time constraints of the slab have to be applied to the system matrix, the solution vector and the right-hand side vector. The space-time hanging node constraints have to be condensed in the solution vector after solving the linear system for all degrees of freedom on the slab.

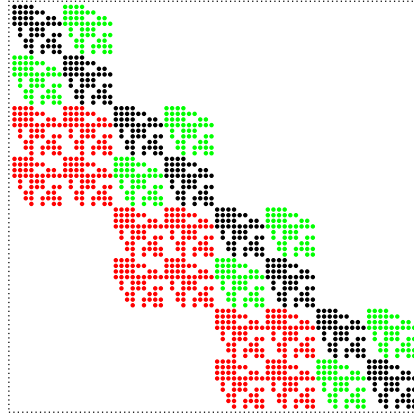


Figure 4.3: Sparsity pattern for the primal operator on a slab for cG(1)-dG(1) with 4 mesh cells in space and 4 mesh cells in time before condensing the Dirichlet nodes. The blocks having black dots correspond to a classical sparsity pattern for one degree of freedom in time. The blocks with green dots are additional couplings between the two time basis functions on a temporal cell. The blocks with red dots are additional couplings from the temporal jump trace operator between two time cells.

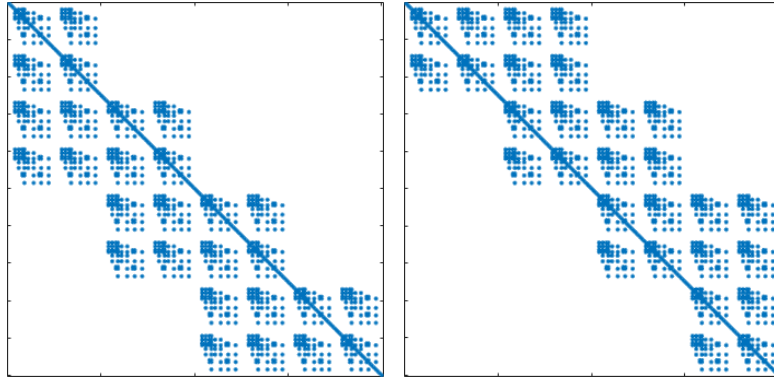


Figure 4.4: Primal and dual operator matrix sparsity patterns on a slab for cG(1)-dG(1) on 16 cells in space and 4 cells in time after condensing the Dirichlet nodes.

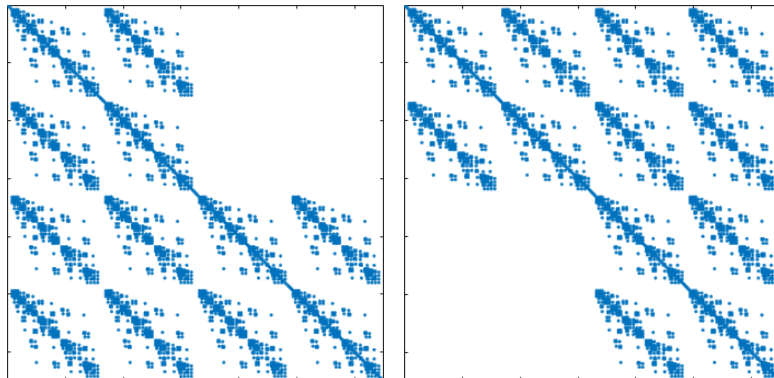


Figure 4.5: Primal and dual operator matrix sparsity patterns on a slab for cG(1)-dG(1) on 64 cells in space and 2 cells in time after condensing the Dirichlet nodes.

5 Algorithm

Here we present the multirate in time adaptive algorithm, give the definition of the (localized) error indicators and explain the approximation techniques used for the weights occurring within these indicators. Our space-time adaptivity strategy uses the following algorithm.

Algorithm: goal-oriented multirate space-time adaptivity

Initialization: Generate the initial space-time slabs $Q_n^1 = \mathcal{T}_{h,n}^1 \times \mathcal{T}_{\tau,n}^1, n = 1, \dots, N^1$, as well as $Q_n^{F,1} = \mathcal{T}_{h,n}^{F,1} \times \mathcal{T}_{\sigma,n}^{F,1}, n = 1, \dots, N^{F,1}, N^{F,1} \leq N^1$, for the transport and Stokes flow problem, respectively, where we restrict $\mathcal{T}_{\sigma,n}^1, \mathcal{T}_{\sigma,n}^{F,1}$ to consist of only one cell in time for each slab.

DWR-loop $\ell = 1, \dots$:

1. **Find the solutions** $\{v_{\sigma h}, p_{\sigma h}\} \in Y_{\sigma h^F}^{\text{dG}(0),p}$ of the Stokes flow problem (2.18).
2. **Find the primal solution** $u_{\tau h} \in X_{\tau h}^{\text{dG}(r),p}$ of the stabilized transport problem (2.15).
3. **Break if the goal yields convergence.**
4. **Find the dual solution** $z_{\tau h} \in X_{\tau h}^{\text{dG}(r),q}, q > p$, of the dual transport problem (3.4c).
5. **Evaluate the localized a posteriori space-time error indicators** η_h and η_τ given by Eq. (5.2) and (5.1), respectively, for the transport problem.
6. Refine the temporal and spatial meshes of the **transport** problem as follows:
 - (i) **If** $|\eta_\tau^\ell| > \omega |\eta_h^\ell|, \omega \geq 1$:
Mark the slabs $Q_{\tilde{n}}^\ell, \tilde{n} \in \{1, \dots, N^\ell\}$, **for temporal refinement** if the corresponding $\eta_{\tau}^{\tilde{n},\ell}$ is in the set of $\theta_\tau^{\text{top}}, 0 \leq \theta_\tau^{\text{top}} \leq 1$, percent of the worst indicators.
 - (ii) **Else if** $|\eta_h^\ell| > \omega |\eta_\tau^\ell|$:
Mark the cells $\tilde{K} \in \mathcal{T}_{h,n}^\ell$ **for spatial refinement** if the corresponding $\eta_h^{n,\ell}|_{\tilde{K}}$ is in the set of $\theta_{h,1}^{\text{top}}$ or $\theta_{h,2}^{\text{top}}$ (for a slab that is or is not marked for temporal refinement), $0 \leq \theta_{h,1}^{\text{top}} \leq \theta_{h,2}^{\text{top}} \leq 1$, percent of the worst indicators, **or**, respectively, mark **for spatial coarsening** if $\eta_h^{n,\ell}|_{\tilde{K}}$ is in the set of $\theta_h^{\text{bottom}}, 0 \leq \theta_h^{\text{bottom}} \leq 1$, percent of the best indicators.
 - (iii) **Else:**
Mark the slabs $Q_{\tilde{n}}^\ell$ **for temporal refinement** as well as **mark the cells** $\tilde{K} \in \mathcal{T}_{h,n}^\ell$ **for spatial coarsening and refinement** as described in Step 6(i) and Step 6(ii), respectively.
 - (iv) **Execute spatial adaptations** on all slabs of the transport problem under the use of mesh smoothing operators.
 - (v) **Execute temporal refinement** on all slabs of the transport problem.
7. **If** $\|v - v_{\sigma h}\|_{(0,T) \times \Omega} > \|u - u_{\tau h}\|_{(0,T) \times \Omega}$:
Refine the spatial and temporal mesh of the **Stokes flow** problem globally.
8. Increase ℓ to $\ell + 1$ and return to Step 1.

Regarding this algorithm, we note the following issues.

Remark 5.1

- For the spatial discretization of the Stokes flow problem we are using Taylor-Hood elements Q_p/Q_{p-1} , $p \geq 2$.
- Within the Steps 2, 4 and 5 of the algorithm, the computed convection field $\mathbf{v}_{\sigma h}$ of the Stokes problem is interpolated to the adaptively refined spatial and temporal triangulation of the space-time slabs.
- Our simulation tools of the DTM++ project are frontend solvers for the deal.II library; cf. [9].
- Technical details of the implementation are given in [8, 20].

In the following, we give some details regarding the localization of the error representations that are derived in Thm. 3.2. Their practical realization and the definition of error indicators η_τ and η_h is obtained by neglecting the remainder terms \mathcal{R}_τ and \mathcal{R}_h of the result given in Thm. 3.2 and splitting the resulting quantities into elementwise contributions.

$$\begin{aligned}
J(u) - J(u_\tau) &\doteq \frac{1}{2} \rho_t^{n,\ell}(u_\tau)(z - \tilde{z}_\tau) + \frac{1}{2} \rho_t^{*,n}(u_\tau, z_\tau)(u - \tilde{u}_\tau) \\
&\quad + \frac{1}{2} \mathcal{D}'_{\tau}{}^{n,\ell}(u_\tau, z_\tau)(\tilde{u}_\tau - u_\tau, \tilde{z}_\tau - z_\tau) + \mathcal{D}_{\tau h}^{n,\ell}(u_{\tau h}, z_{\tau h}) \\
&=: \eta_\tau^\ell = \sum_{n=1}^{N^\ell} \eta_\tau^{n,\ell}, \tag{5.1}
\end{aligned}$$

$$\begin{aligned}
J(u_\tau) - J(u_{\tau h}) &\doteq \frac{1}{2} \rho_t^{n,\ell}(u_{\tau h})(z_\tau - \tilde{z}_{\tau h}) + \frac{1}{2} \rho_t^{*,n,\ell}(u_{\tau h}, z_{\tau h})(u_\tau - \tilde{u}_{\tau h}) \\
&\quad + \frac{1}{2} \mathcal{D}'_{\tau h}{}^{n,\ell}(u_{\tau h}, z_{\tau h})(\tilde{u}_{\tau h} - u_{\tau h}, \tilde{z}_{\tau h} - z_{\tau h}) + \mathcal{D}_{\tau h}^{n,\ell}(u_{\tau h}, z_{\tau h}) \\
&=: \eta_h^\ell = \sum_{n=1}^{N^\ell} \eta_h^{n,\ell} = \sum_{n=1}^{N^\ell} \sum_{K \in \mathcal{T}_h^{n,\ell}} \eta_{h,K}^{n,\ell}. \tag{5.2}
\end{aligned}$$

To compute the error indicators η_τ and η_h we replace all unknown solutions by the approximated fully discrete solutions $u_{\tau h} \in X_{\tau h}^{\text{dG}(r),p}$, $z_{\tau h} \in X_{\tau h}^{\text{dG}(r),q}$, with $p < q$, and $\mathbf{v}_{\sigma h} \in Y_{\sigma h^F}^{\text{dG}(0),p_v}$, $p_v \geq 2$, whereby the arising weights are approximated in the following way.

- Approximate the temporal weights $u - \tilde{u}_\tau$ and $z - \tilde{z}_\tau$, respectively, by means of a higher-order extrapolation using Gauss-Lobatto quadrature points given by

$$\begin{aligned}
u - \tilde{u}_\tau &\approx E_\tau^{(r+1)} u_{\tau h} - u_{\tau h}, \\
z - \tilde{z}_\tau &\approx E_\tau^{(r+1)} z_{\tau h} - z_{\tau h},
\end{aligned}$$

using an extrapolation in time operator $E_\tau^{(r+1)}$ that acts on a time cell of length τ_K and lifts the solution to a piecewise polynomial of degree $(r+1)$ in time. This approximation technique is a new approach compared to our previous work [20, Sec. 4], where a higher-order finite element approximation was used, and is done for the purpose to reduce numerical costs solving the dual problem.

- Approximate the spatial weights $u_\tau - \tilde{u}_{\tau h}$ and $z_\tau - \tilde{z}_{\tau h}$ by means of a patch-wise higher-order interpolation and a higher-order finite elements approach, respectively, given by

$$\begin{aligned} u_\tau - \tilde{u}_{\tau h} &\approx I_{2h}^{(2p)} u_{\tau h} - u_{\tau h}, \\ z_\tau - \tilde{z}_{\tau h} &\approx z_{\tau h} - R_h^p z_{\tau h}, \end{aligned}$$

using an interpolation in space operator $I_{2h}^{(2p)}$ and an restriction in space operator R_h^p that are described in detail in our work [20, Sec. 4].

6 Numerical Examples

In the following section we study the convergence, computational efficiency and stability of the introduced goal-oriented DWR based adaptivity approach for the coupled transport and Stokes flow problem. The first example given in Sec. 6.1 is an academic test problem with given analytical solutions to study the convergence behavior of the two subproblems and, in particular, the coupling between them. The second example given in Sec. 6.2 serves to demonstrate the performance properties of the algorithm with regard to adaptive mesh refinement in space and time. Finally, the third example in Sec. 6.3 is motivated by problem of physical relevance in which we simulate a convection-dominated transport with goal-oriented adaptivity of a species through a channel with a constraint.

6.1 Example 1 (Higher-order space-time convergence studies)

In a first numerical example we study the space-time higher-order convergence behavior to validate the correctness of the higher-order implementations in space and time. Therefore, we consider the two cases of a solely solved Stokes flow problem as well as a non-stabilized solved convection-diffusion-reaction transport problem coupled with this Stokes equation via the convection field solution $\mathbf{v}_{\sigma h}$. The latter may be compared to the results of a solely solved transport equation with a constant convection field $\mathbf{v} = (2, 3)^\top$ published in our work [20, Example 1]. For this purpose, we investigate problem (2.3) with the given analytical solution

$$\begin{aligned} \mathbf{v}(\mathbf{x}, t) &:= \begin{pmatrix} \sin(t) \sin^2(\pi x_1) \sin(\pi x_2) \cos(\pi x_2) \\ -\sin(t) \sin(\pi x_1) \cos(\pi x_1) \sin^2(\pi x_2) \end{pmatrix}, \\ p(\mathbf{x}, t) &:= \sin(t) \sin(\pi x_1) \cos(\pi x_1) \sin(\pi x_2) \cos(\pi x_2), \end{aligned} \quad (6.1)$$

with $\mathbf{x} = (x_1, x_2)^\top \in \mathbb{R}^2$, $t \in \mathbb{R}$ and $\nabla \cdot \mathbf{v} = 0$. The viscosity is set to $\nu = 0.5$. The problem is defined on $Q = \Omega \times I := (0, 1)^2 \times (0, 1]$. The initial and boundary conditions are given as

$$\mathbf{v} = 0 \text{ on } \Sigma_0 = \Omega \times \{0\}, \quad \mathbf{v} = 0 \text{ on } \Sigma_D = \partial\Omega \times (0, 1),$$

and the volume force term \mathbf{f} is calculated from the given analytical solution (6.1) and Eq. (2.3). This example is a typical test problem for time-dependent incompressible flow and can be found, for instance, in [32, Example 1].

For the following test settings, the solution $\{\mathbf{v}, p\}$ is approximated with the space-time higher-order methods $\{\text{cG}(2)\text{-dG}(2), \text{cG}(1)\text{-dG}(2)\}$ and $\{\text{cG}(3)\text{-dG}(3), \text{cG}(2)\text{-dG}(3)\}$, respectively. Due to the same polynomial orders of the spatial and temporal discretizations with respect to the convection field \mathbf{v} , and lower polynomial order in space compared to in time with respect to the pressure variable p , we expect experimental orders of convergence (EOC $:= -\log_2(\|e\|_\ell / \|e\|_{\ell-1})$) for the convection field \mathbf{v} of $\text{EOC}^{2,2} \approx 3$ for the $\text{cG}(2)\text{-dG}(2)$ method and $\text{EOC}^{3,3} \approx 4$ for the $\text{cG}(3)\text{-dG}(3)$ method, as well as experimental orders of convergence for the pressure variable p of $\text{EOC}^{1,2} \approx 2$ for the $\text{cG}(1)\text{-dG}(2)$ method and $\text{EOC}^{2,3} \approx 3$

for the cG(2)-dG(3) method for a global refinement convergence test. The results are given by Tab. 6.1 and nicely confirm our expected results for the respective spatial and temporal discretizations.

| ℓ | N | N_K | $N_{\text{DoF}}^{\text{tot}}$ | $\ \mathbf{v} - \mathbf{v}_{\sigma h}^{2,2}\ $ | EOC | $\ p - p_{\sigma h}^{1,2}\ $ | EOC |
|--------|-----|-------|-------------------------------|--|------|------------------------------|------|
| 1 | 4 | 16 | 2244 | 3.7974e-03 | — | 2.0593e-02 | — |
| 2 | 8 | 64 | 15816 | 4.4945e-04 | 3.08 | 2.5898e-03 | 2.99 |
| 3 | 16 | 256 | 118416 | 5.5129e-05 | 3.03 | 5.5087e-04 | 2.23 |
| 4 | 32 | 1024 | 915744 | 6.8603e-06 | 3.01 | 1.3405e-04 | 2.04 |
| 5 | 64 | 4096 | 7201344 | 8.5697e-07 | 3.00 | 3.3291e-05 | 2.01 |
| 6 | 128 | 16384 | 57115776 | 1.0713e-07 | 3.00 | 8.3039e-06 | 2.00 |
| 7 | 256 | 65536 | 454953216 | 1.3394e-08 | 3.00 | 2.0740e-06 | 2.00 |

| ℓ | N | N_K | $N_{\text{DoF}}^{\text{tot}}$ | $\ \mathbf{v} - \mathbf{v}_{\sigma h}^{3,3}\ $ | EOC | $\ p - p_{\sigma h}^{2,3}\ $ | EOC |
|--------|-----|-------|-------------------------------|--|------|------------------------------|------|
| 1 | 4 | 16 | 6704 | 3.0085e-04 | — | 3.6349e-03 | — |
| 2 | 8 | 64 | 49248 | 1.9122e-05 | 3.98 | 4.9603e-04 | 2.87 |
| 3 | 16 | 256 | 377024 | 1.2073e-06 | 3.99 | 4.6902e-05 | 3.40 |
| 4 | 32 | 1024 | 2949504 | 7.5829e-08 | 3.99 | 4.6449e-06 | 3.34 |
| 5 | 64 | 4096 | 23331584 | 4.7494e-09 | 4.00 | 5.3029e-07 | 3.13 |
| 6 | 128 | 16384 | 185599488 | 2.9712e-10 | 4.00 | 6.4815e-08 | 3.03 |

Table 6.1: Global convergence for $\mathbf{v}_{\sigma h}^{2,2}, p_{\sigma h}^{1,2}$ in a cG(2)-dG(2), cG(1)-dG(2) and $\mathbf{v}_{\sigma h}^{3,3}, p_{\sigma h}^{2,3}$ in a cG(3)-dG(3), cG(2)-dG(3) primal approximation for a time-dependent Stokes flow problem for Sec. 6.1. ℓ denotes the refinement level, N the total cells in time, N_K the cells in space on a slab, $N_{\text{DoF}}^{\text{tot}}$ the total space-time degrees of freedom, $\|\cdot\|$ the global $L^2(L^2)$ -norm error and EOC the experimental order of convergence.

The second part of the first example now serves to verify the higher-order implementation of the coupled problem. Therefore, the convection-diffusion-reaction transport problem (2.1) is coupled with the Stokes flow problem (2.3) via the convection field solution $\mathbf{v}_{\sigma h}$, using the exact solution \mathbf{v} given by Eq. (6.1). More precisely, we study problem (2.1) with the given analytical solution

$$\begin{aligned}
u(\mathbf{x}, t) &:= u_1 \cdot u_2, \quad \mathbf{x} = (x_1, x_2)^\top \in \mathbb{R}^2 \text{ and } t \in \mathbb{R}, \\
u_1(\mathbf{x}, t) &:= (1 + a \cdot ((x_1 - m_1(t))^2 + (x_2 - m_2(t))^2))^{-1}, \\
u_2(t) &:= v_1(t) \cdot s \cdot \arctan(v_2(t)),
\end{aligned} \tag{6.2}$$

with $m_1(t) := \frac{1}{2} + \frac{1}{4} \cos(2\pi t)$ and $m_2(t) := \frac{1}{2} + \frac{1}{4} \sin(2\pi t)$, and, $v_1(\hat{t}) := -1$, $v_2(\hat{t}) := 5\pi \cdot (4\hat{t} - 1)$, for $\hat{t} \in [0, 0.5)$ and $v_1(\hat{t}) := 1$, $v_2(\hat{t}) := 5\pi \cdot (4(\hat{t} - 0.5) - 1)$, for $\hat{t} \in [0.5, 1)$, $\hat{t} = t - k$, $k \in \mathbb{N}_0$, and, scalars $a = 50$ and $s = -\frac{1}{3}$. The (analytic) solution (6.2) mimics a counterclockwise rotating cone which additionally changes its height and orientation over the period $T = 1$. Precisely, the orientation of the cone switches from negative to positive while passing $t = 0.25$ and from positive to negative while passing $t = 0.75$. The inhomogeneous Dirichlet boundary condition, the inhomogeneous initial condition and the right-hand side forcing term g , are calculated from the given analytic solution (6.2) and Eq. (2.1), where the latter uses the exact Stokes solution \mathbf{v} given by Eq. (6.1). Moreover, we note that the assembly of the transport system matrix uses the approximated fully-discrete Stokes solution $\mathbf{v}_{\sigma h}$ of (2.18) that has to be transferred to the spatial and temporal mesh of the transport problem, cf. Rem. 5.1 in Sec. 5.

Since we study the global space-time refinement behavior here, we restrict the convection-diffusion-reaction transport problem to a non-stabilized case, i.e. we set $\delta_0 := 0$ within the local SUPG stabilization parameter $\delta_K = \delta_0 \cdot h_K$, where h_K denotes the cell diameter of the spatial mesh cell K . Moreover, we set the diffusion coefficient $\varepsilon = 1$ and choose a

constant reaction coefficient $\alpha = 1$. The global space-time refinement behavior is illustrated

| ℓ | N | N_K | $\ u - u_{\tau h}^{1,1}\ $ | EOC | N | N_K | $\ v - v_{\sigma h}^{2,0}\ $ | EOC |
|--------|-----|-------|----------------------------|------|-----|-------|------------------------------|------|
| 1 | 4 | 4 | 8.4766e-02 | — | 4 | 16 | 4.5783e-03 | — |
| 2 | 8 | 16 | 2.7780e-02 | 1.61 | 8 | 64 | 1.7196e-03 | 1.41 |
| 3 | 16 | 64 | 9.1450e-03 | 1.60 | 16 | 256 | 9.9383e-04 | 0.79 |
| 4 | 32 | 256 | 3.0372e-03 | 1.59 | 32 | 1024 | 5.6228e-04 | 0.82 |
| 5 | 64 | 1024 | 7.7372e-04 | 1.97 | 64 | 4096 | 3.0374e-04 | 0.89 |
| 6 | 128 | 4096 | 1.9407e-04 | 2.00 | 128 | 16384 | 1.5868e-04 | 0.94 |
| 7 | 256 | 16384 | 4.9596e-05 | 1.97 | 256 | 65536 | 1.5868e-04 | 0.94 |

| ℓ | N | N_K | $\ u - u_{\tau h}^{2,2}\ $ | EOC | N | N_K | $\ v - v_{\sigma h}^{3,0}\ $ | EOC |
|--------|-----|-------|----------------------------|------|-----|-------|------------------------------|------|
| 1 | 4 | 1 | 9.9045e-02 | — | 4 | 4 | 7.6009e-03 | — |
| 2 | 8 | 4 | 4.8261e-02 | 1.04 | 8 | 16 | 1.7488e-03 | 2.12 |
| 3 | 16 | 16 | 6.0634e-03 | 2.99 | 16 | 64 | 9.9237e-04 | 0.82 |
| 4 | 32 | 64 | 1.0858e-03 | 2.48 | 32 | 256 | 5.6213e-04 | 0.82 |
| 5 | 64 | 256 | 1.5131e-04 | 2.84 | 64 | 1024 | 3.0373e-04 | 0.89 |
| 6 | 128 | 1024 | 2.0859e-05 | 2.86 | 128 | 4096 | 1.5868e-04 | 0.94 |
| 7 | 256 | 4096 | 2.7041e-06 | 2.95 | 256 | 16384 | 8.1226e-05 | 0.97 |

Table 6.2: Global convergence for $v_{\sigma h}^{2,2}, p_{\sigma h}^{1,2}$ in a cG(2)-dG(2), cG(1)-dG(2) and $v_{\sigma h}^{3,3}, p_{\sigma h}^{2,3}$ in a cG(3)-dG(3), cG(2)-dG(3) primal approximation for a time-dependent Stokes flow problem for Sec. 6.1. ℓ denotes the refinement level, N the total cells in time, N_K the cells in space on a slab, $N_{\text{DoF}}^{\text{tot}}$ the total space-time degrees of freedom, $\|\cdot\|$ the global $L^2(L^2)$ -norm error and EOC the experimental order of convergence.

by Tab. 6.2 and nicely confirms our results with respect to the expected EOCs for the solely solved transport problem obtained in [20, Example 1], cf. columns four and five of Tab. 6.2. Furthermore, with regard to the EOCs of the Stokes solution, we note that both approximations cG(2)-dG(0) as well as cG(3)-dG(0) are restricted through the lowest order approximation in time, cf. columns eight and nine of Tab. 6.2.

6.2 Example 2 (Space-time adaptivity studies for the coupled problem)

The second example serves to study the goal-oriented space-time adaptivity behavior of our algorithm introduced in Sec. 5. More precisely, the transport problem is adaptively refined in space and time using an approximated Stokes solution $v_{\sigma h}$ on a coarser global refined mesh in space and time. The initial space-time meshes of the transport problem are once more refined compared to the initial meshes of the Stokes flow problem, cf. the first row of Tab. 6.3. The temporal and spatial mesh of the Stokes flow problem is refined globally if the global $L^2(L^2)$ -error $\|v - v_{\sigma h}^{2,0}\|$ is larger than its counterpart $\|u - u_{\tau h}^{1,0}\|$ or rather $\|u - u_{\tau h}^{1,1}\|$ for the transport problem (cf. columns five and nine of Tab. 6.3 and Tab. 6.4, respectively.).

We study problem (2.1) and (2.3) with the given analytical solutions (6.2) and (6.1), respectively, with the same settings as given in Sec. 6.1. Our target quantity for the transport problem is chosen to control the global $L^2(L^2)$ -error of e , $e = u - u_{\tau h}$, in space and time, given by

$$J(\varphi) = \frac{1}{\|e\|_{(0,T) \times \Omega}} \int_I (\varphi, e) dt, \quad \text{with } \|\cdot\|_{(0,T) \times \Omega} = \left(\int_I (\cdot, \cdot) dt \right)^{\frac{1}{2}}. \quad (6.3)$$

The tuning parameters of the goal-oriented adaptive Algorithm given in Sec. 5 are chosen here in a way to balance automatically the potential misfit of the spatial and temporal errors as

$$\theta_h^{\text{top}} = 0.5 \cdot \left| \frac{\eta_h}{|\eta_h| + |\eta_\tau|} \right|, \quad \theta_h^{\text{bottom}} = 0 \quad \text{and} \quad \theta_\tau^{\text{top}} = 0.5 \cdot \left| \frac{\eta_\tau}{|\eta_h| + |\eta_\tau|} \right|.$$

For measuring the accuracy of the error estimator, we will study the so-called effectivity index given by

$$\mathcal{I}_{\text{eff}} = \left| \frac{\eta_\tau + \eta_h}{J(u) - J(u_{\tau h})} \right| \quad (6.4)$$

as the ratio of the estimated error over the exact error. Desirably, the index \mathcal{I}_{eff} should be close to one.

In Tab. 6.3 and Tab. 6.4 we present the development of the total discretization error $J(e) = \|e\|_{(0,T) \times \Omega}$ for (6.3), the approximated spatial and temporal error estimators η_h and η_τ as well as the effectivity index \mathcal{I}_{eff} during an adaptive refinement process for two different primal and dual solution pairings $\{u_{\tau h}, z_{\tau h}\}$: cG(1)-dG(0)/cG(2)-dG(0), cG(1)-dG(1)/cG(2)-dG(1) of the transport problem. Moreover, the development of the total discretization error $\|\mathbf{v} - \mathbf{v}_{\sigma h}^{2,0}\|$ for the Stokes flow solution on a global refined mesh in space and time and the corresponding number of slabs and spatial cells is displayed. Thereby, $\mathbf{v}_{\sigma h}^{2,0}$ corresponds to a Stokes solution approximation in a cG(2)-dG(0) discretization. We use an approximation of the temporal weights by a higher-order extrapolation strategy using Gauss-Lobatto quadrature points. Here and in the following, ℓ denotes the refinement level or DWR loop, N or N^F the total cells in time, N_K^{max} or $N_K^{F,\text{max}}$ the number of spatial cells on the finest spatial mesh within the current loop, and $N_{\text{DoF}}^{\text{tot}}$ or $N_{\text{DoF}}^{F,\text{tot}}$ the total space-time degrees of freedom of the transport or Stokes flow problem, respectively.

Regarding the accuracy of the underlying error estimator, as given by the last column of Tab. 6.3 or Tab. 6.4, respectively, we observe a good quantitative estimation of the discretization error as the respective effectivity index increases getting close to one. With regard to efficiency reasons for a space-time adaptive algorithm, it is essential to ensure an equilibrated reduction of the temporal as well as spatial discretization error, cf. [32, Sec. 3.3]. Referring to this, we point out a good equilibration of the spatial and temporal error indicators η_h and η_τ in the course of the refinement process (columns ten and eleven of Tab. 6.3 and Tab. 6.4).

| DWR ℓ | Stokes Flow | | | | | Transport | | | | | | |
|---------------|-------------|----------------------|---------------------------------|--|-----|--------------------|-------------------------------|-------------------|-----------|-------------|-----------------|----------------------------|
| | N^F | $N_K^{F,\text{max}}$ | $N_{\text{DoF}}^{F,\text{tot}}$ | $\ \mathbf{v} - \mathbf{v}_{\sigma h}^{2,0}\ $ | N | N_K^{max} | $N_{\text{DoF}}^{\text{tot}}$ | $\ e^{1,0,2,0}\ $ | η_h | η_τ | $\eta_{\tau h}$ | \mathcal{I}_{eff} |
| 1 | 5 | 4 | 295 | 1.966e-02 | 10 | 16 | 250 | 5.245e-02 | 4.270e-03 | 3.335e-04 | 4.604e-03 | 0.09 |
| 2 | | | | 1.966e-02 | 10 | 40 | 438 | 4.681e-02 | 7.122e-04 | 3.547e-03 | 4.260e-03 | 0.09 |
| 3 | | | | 1.966e-02 | 14 | 40 | 616 | 1.729e-02 | 3.587e-03 | 1.594e-03 | 5.180e-03 | 0.30 |
| 4 | 10 | 16 | 1870 | 4.099e-03 | 19 | 88 | 1913 | 1.100e-02 | 1.607e-03 | 3.784e-03 | 5.391e-03 | 0.49 |
| 5 | | | | 4.099e-03 | 26 | 160 | 4074 | 7.139e-03 | 6.659e-04 | 3.638e-03 | 4.304e-03 | 0.60 |
| 6 | | | | 4.099e-03 | 36 | 160 | 5534 | 5.036e-03 | 9.436e-04 | 2.585e-03 | 3.528e-03 | 0.70 |
| 7 | | | | 4.099e-03 | 50 | 268 | 11954 | 3.439e-03 | 4.237e-04 | 2.146e-03 | 2.570e-03 | 0.75 |
| 8 | 20 | 64 | 13180 | 9.684e-04 | 70 | 268 | 16752 | 2.585e-03 | 5.376e-04 | 1.453e-03 | 1.991e-03 | 0.77 |
| 9 | | | | 9.684e-04 | 98 | 448 | 37900 | 1.844e-03 | 2.343e-04 | 1.183e-03 | 1.417e-03 | 0.77 |
| 10 | 20 | 64 | 13180 | 9.684e-04 | 137 | 448 | 52937 | 1.402e-03 | 2.908e-04 | 8.384e-04 | 1.129e-03 | 0.81 |

Table 6.3: Adaptive refinement in the transport problem including effectivity indices for goal quantity (6.3), with $\varepsilon = 1, \delta_0 = 0$, and $\omega = 3$ for Sec. 6.2 using a Stokes solution $\mathbf{v}_{\sigma h}^{2,0}$ corresponding to a cG(2)-dG(0) approximation on a global refined mesh in space and time. $e^{1,0,2,0}$ corresponds to the adaptive solution approximation $u_{\tau h}^{1,0}$ in cG(1)-dG(0) and dual solution approximation $z_{\tau h}^{2,0}$ in cG(2)-dG(0).

Finally, in Fig. 6.1 we visualize exemplarily the distribution of the adaptively determined time cell lengths τ_K of $\mathcal{T}_{\tau,n}$, used for the transport problem, as well as the distribution of the globally determined time cell lengths σ_K of $\mathcal{T}_{\sigma,n}$, used for the Stokes flow problem, over the whole time interval I for different DWR refinement loops, corresponding to Tab. 6.3. The initial temporal meshes for the transport and Stokes flow problem are chosen fulfilling the requirements presented in Sec. 2.2 and Fig. 2.1. While the time steps for the transport problem become smaller when the cone is changing its orientation ($t = 0.25$ and $t = 0.75$), the time steps for the Stokes flow problem stay comparatively large in the course of the refinement

| DWR | Stokes Flow | | | | Transport | | | | | | | |
|--------|-------------|----------------|---------------------------------|------------------------------|-----------|--------------|-------------------------------|-------------------|-----------|-------------|-----------------|----------------------------|
| ℓ | N^F | $N_K^{F,\max}$ | $N_{\text{DoF}}^{F,\text{tot}}$ | $\ v - v_{\sigma h}^{2,0}\ $ | N | N_K^{\max} | $N_{\text{DoF}}^{\text{tot}}$ | $\ e^{1,1,2,1}\ $ | η_h | η_τ | $\eta_{\tau h}$ | \mathcal{I}_{eff} |
| 1 | 5 | 4 | 295 | 1.966e-02 | 20 | 16 | 1000 | 2.547e-02 | 2.139e-02 | 1.231e-04 | 2.126e-02 | 0.83 |
| 2 | | | | 1.966e-02 | 20 | 28 | 1640 | 1.158e-02 | 1.279e-02 | 4.406e-03 | 1.719e-02 | 1.48 |
| 3 | 10 | 16 | 1870 | 4.099e-03 | 20 | 76 | 2956 | 7.730e-03 | 3.986e-03 | 5.234e-03 | 9.220e-03 | 1.19 |
| 4 | | | | 4.099e-03 | 28 | 124 | 6468 | 4.340e-03 | 3.634e-03 | 4.309e-03 | 7.943e-03 | 1.83 |
| 5 | | | | 4.099e-03 | 39 | 172 | 11694 | 2.840e-03 | 2.314e-03 | 3.446e-03 | 5.760e-03 | 2.02 |
| 6 | 20 | 64 | 13180 | 9.684e-04 | 54 | 232 | 20348 | 1.945e-03 | 8.625e-04 | 3.172e-03 | 4.035e-03 | 2.07 |
| 7 | | | | 9.684e-04 | 64 | 232 | 24600 | 1.889e-03 | 2.207e-04 | 2.273e-03 | 2.052e-03 | 1.08 |
| 8 | | | | 9.684e-04 | 75 | 232 | 28022 | 1.871e-03 | 5.367e-05 | 2.367e-03 | 2.313e-03 | 1.23 |
| 9 | | | | 9.684e-04 | 147 | 316 | 66570 | 1.469e-03 | 2.111e-03 | 6.047e-04 | 1.506e-03 | 1.02 |
| 10 | 40 | 256 | 98680 | 4.691e-04 | 283 | 532 | 220298 | 8.416e-04 | 9.537e-04 | 8.517e-05 | 8.685e-04 | 1.03 |

Table 6.4: Adaptive refinement in the transport problem including effectivity indices for goal quantity (6.3), with $\varepsilon = 1, \delta_0 = 0$, and $\omega = 3$ for Sec. 6.2 using a Stokes solution $v_{\sigma h}^{2,0}$ corresponding to a cG(2)-dG(0) approximation on a global refined mesh in space and time. $e^{1,1,2,1}$ corresponds to the adaptive solution approximation $u_{\tau h}^{1,0}$ in cG(1)-dG(1) and dual solution approximation $z_{\tau h}^{2,1}$ in cG(2)-dG(1).

process, cf. the last two plots of Fig. 6.1. Away from the time points of orientation change, the temporal mesh of the transport problem is almost equally decomposed. This behavior seems natural for a global acting target quantity (6.3) and nicely confirms our approach of an efficient temporal approximation of a rapidly changing transport coupled with a slowly varying viscous flow.

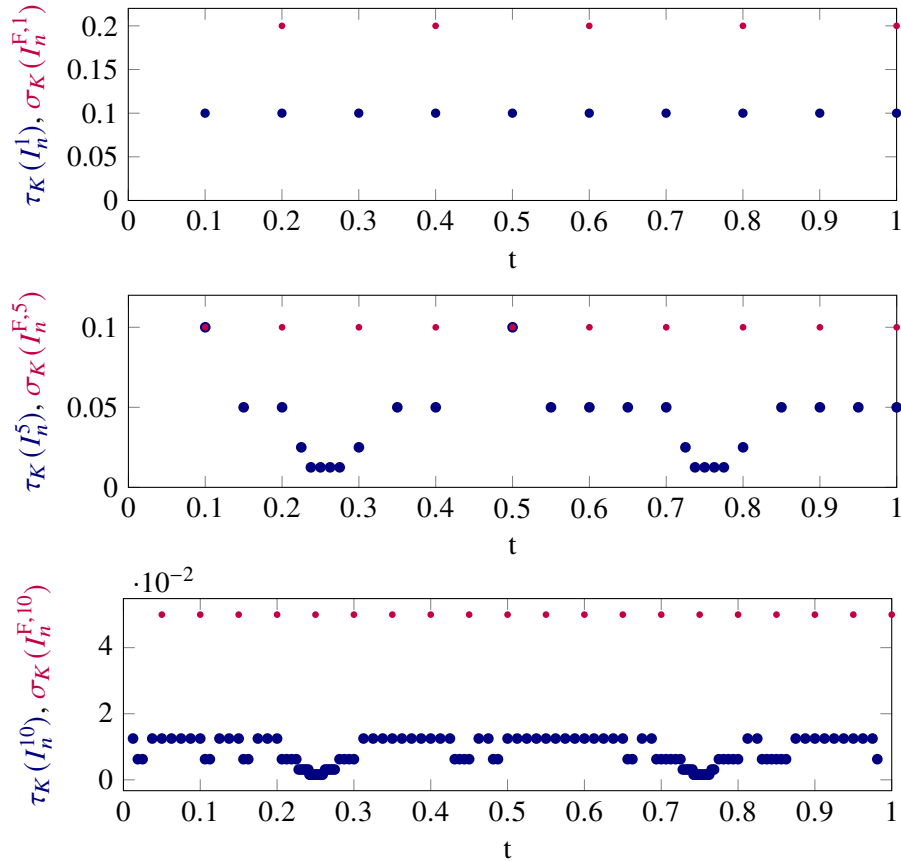


Figure 6.1: Distribution of the temporal step size τ_K of the transport problem (adaptive) and σ_K of the Stokes flow problem (global) over the time interval $I = (0, T]$ for the initial (1) and after 5 and 10 DWR-loops, corresponding to Tab. 6.3.

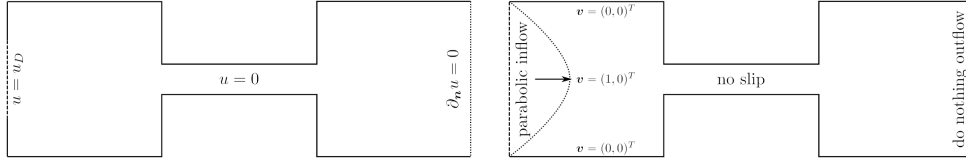


Figure 6.2: Boundary colorization for the convection-diffusion-reaction problem (left) and the coupled Stokes flow problem (right) for Sec. 6.3.

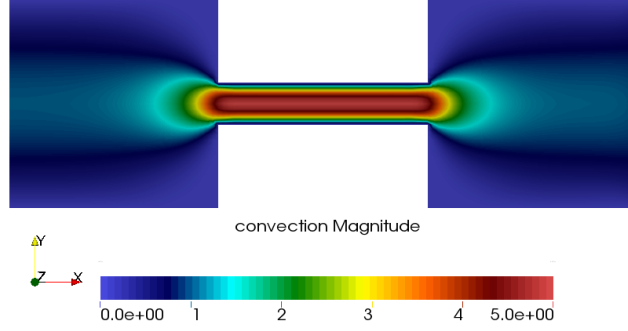


Figure 6.3: Convection $\mathbf{v}_{\sigma h}$ solution of the Stokes problem on one slab with a sufficiently globally refined spatial mesh with Q_2 - Q_1 finite elements for Sec. 6.3. On the left boundary a parabolic inflow profile in the positive x-direction with unit magnitude is prescribed for the convection \mathbf{v} .

6.3 Example 3 (Transport in a channel)

In this example we simulate a convection-dominated transport with goal-oriented adaptivity of a species through a channel with a constraint. The domain and its boundary colorization are presented by Fig. 6.2. Precisely, the spatial domain is composed of two unit squares and a constraint in the middle which restricts the channel height by a factor of 5. Precisely, $\Omega = (-1, 0) \times (-0.5, 0.5) \cup (0, 1) \times (-0.1, 0.1) \cup (1, 2) \times (-0.5, 0.5)$ with an initial cell diameter of $h = \sqrt{2 \cdot 0.025^2}$. The time domain is set to $I = (0, 2.5)$ with an initial $\tau = 0.1$ for the transport and $\sigma = 2.5$ for the Stokes flow problem for the initialization of the slabs for the first loop $\ell = 1$. This choice has been made to compare the results to Example 2 in [20], where a quasi-stationary Stokes flow solution \mathbf{v}_h was used. We approximate the primal solution $u_{\tau h}^{1,0}$ with the cG(1)-dG(0) method, the dual solution $z_{\tau h}^{2,0}$ with the cG(2)-dG(0) method and the Stokes flow solution $\mathbf{v}_{\sigma h}^{2,0}$ with the cG(2)-dG(0) method.

The target quantity is

$$J(u) = \frac{1}{|T| \cdot |\Omega|} \int_I \int_{\Omega} u(\mathbf{x}, t) \, d\mathbf{x} dt. \quad (6.5)$$

The transport of the species, which enters the domain on the left with an inhomogeneous and time-dependent Dirichlet boundary condition and leaves the domain on the right through a homogeneous Neumann boundary condition, is driven by the convection with magnitudes between 0 and 5 as displayed in Fig. 6.3. The diffusion coefficient has the constant and small value of $\varepsilon = 10^{-4}$ and the reaction coefficient is chosen $\alpha = 0.1$. The local SUPG stabilization coefficient is here set to $\delta_K = \delta_0 \cdot h_K$, $\delta_0 = 0$, i.e. a vanishing stabilization here. The initial value function $u_0 = 0$ as well as the forcing term $g = 0$ are homogeneous. The Dirichlet boundary function value is homogeneous on Γ_D except for the line $(-1, -1) \times (-0.4, 0.4)$ and time $0 \leq t \leq 0.2$ where the constant value

$$u(\mathbf{x}, t) = 1$$

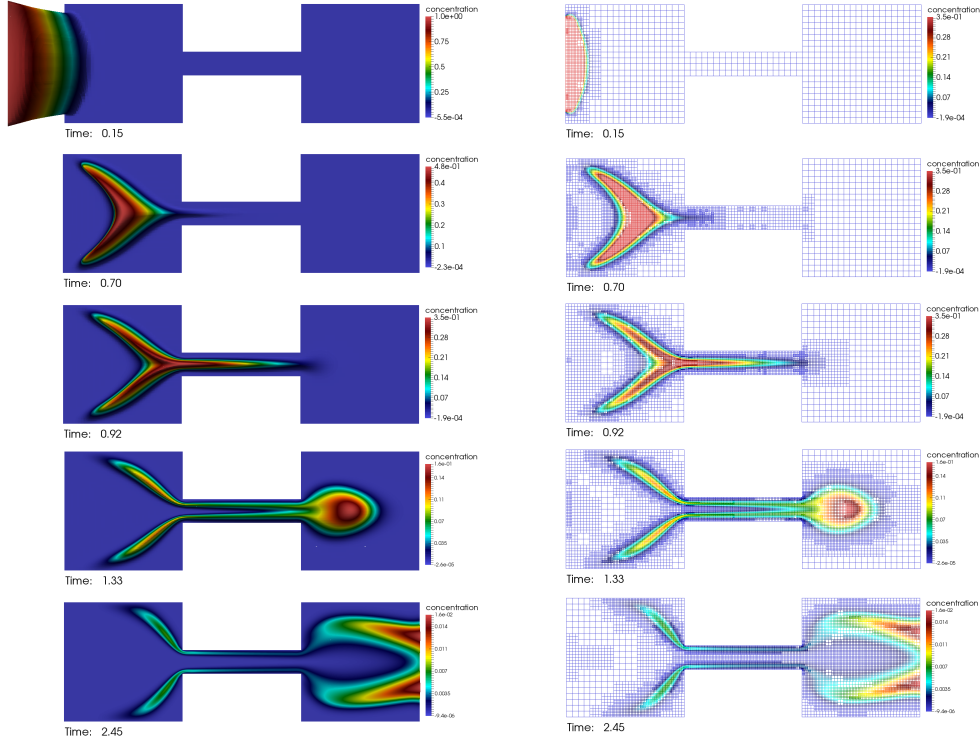


Figure 6.4: Solution profiles and corresponding meshes of loop $\ell = 8$ for Sec. 6.3.

is prescribed on the solution. The viscosity is set to $\nu = 1$. The tuning parameters of the goal-oriented adaptive Algorithm given in Sec. 5 are chosen here in a way to balance automatically the potential misfit of the spatial and temporal errors as $\theta_h^{\text{bottom}} = 0$,

$$\theta_h^{\text{top}} = \frac{1}{2} \cdot \min \left\{ \left| \frac{\eta_h}{|\eta_h| + |\eta_\tau|} \right|, 1 \right\} \quad \text{and} \quad \theta_\tau^{\text{top}} = \frac{1}{2} \cdot \min \left\{ \left| \frac{\eta_\tau}{|\eta_h| + |\eta_\tau|} \right|, 1 \right\}. \quad (6.6)$$

The solution profiles and corresponding adaptive meshes of the primal solution $u_{\tau h}^{1,0}$ of the loop $\ell = 8$ for $t = 0.15$, $t = 0.70$, $t = 0.92$, $t = 1.33$ and $t = 2.45$ are given by Fig. 6.4. The refinement in space is adjusted to the position of the transported species within the channel. It is located to the layers of the transported species, whereas the mesh stays coarse in the non-affected area. In Fig. 6.5 we present a comparative study of the solution profile and corresponding meshes for $t = 0.95$ over the adaptivity loops. For $\ell = 1, 2, 3$ obvious spurious oscillations in the left square and at the beginning of the constriction are existing, which are captured and resolved by the goal-oriented adaptivity by taking spatial mesh refinements along the layers of the transported species within the left square and within the constriction of the channel. For $\ell > 3$ the spatial refinements capture especially the solution profile fronts with strong gradients with a focus on the high-convective middle of the spatial domain. In Fig. 6.6 we visualize the temporal distribution of the transport problem for several DWR-loops. The time cell lengths of the Stokes flow problem is kept fixed with value $\sigma_K = 2.5$ for all DWR-loops here and thus explicitly not displayed. We observe an adaptive refinement in time at the beginning, consistent with the restriction in time of the inflow boundary condition. The closer we get to the final time point T the coarser the temporal mesh is chosen.

The refinement in space and time is automatically balanced due to the dynamic choice of θ_h^{top} and θ_τ^{top} given by (6.6) and is illustrated by Tab. 6.5. Regarding the spatial and temporal error indicators (cf. columns five and six of Tab. 6.5) a good equilibration can be observed within the final loop, whereas in the first step a mismatch occurs resulting in a solely temporal refinement between $\ell = 1$ and $\ell = 2$.

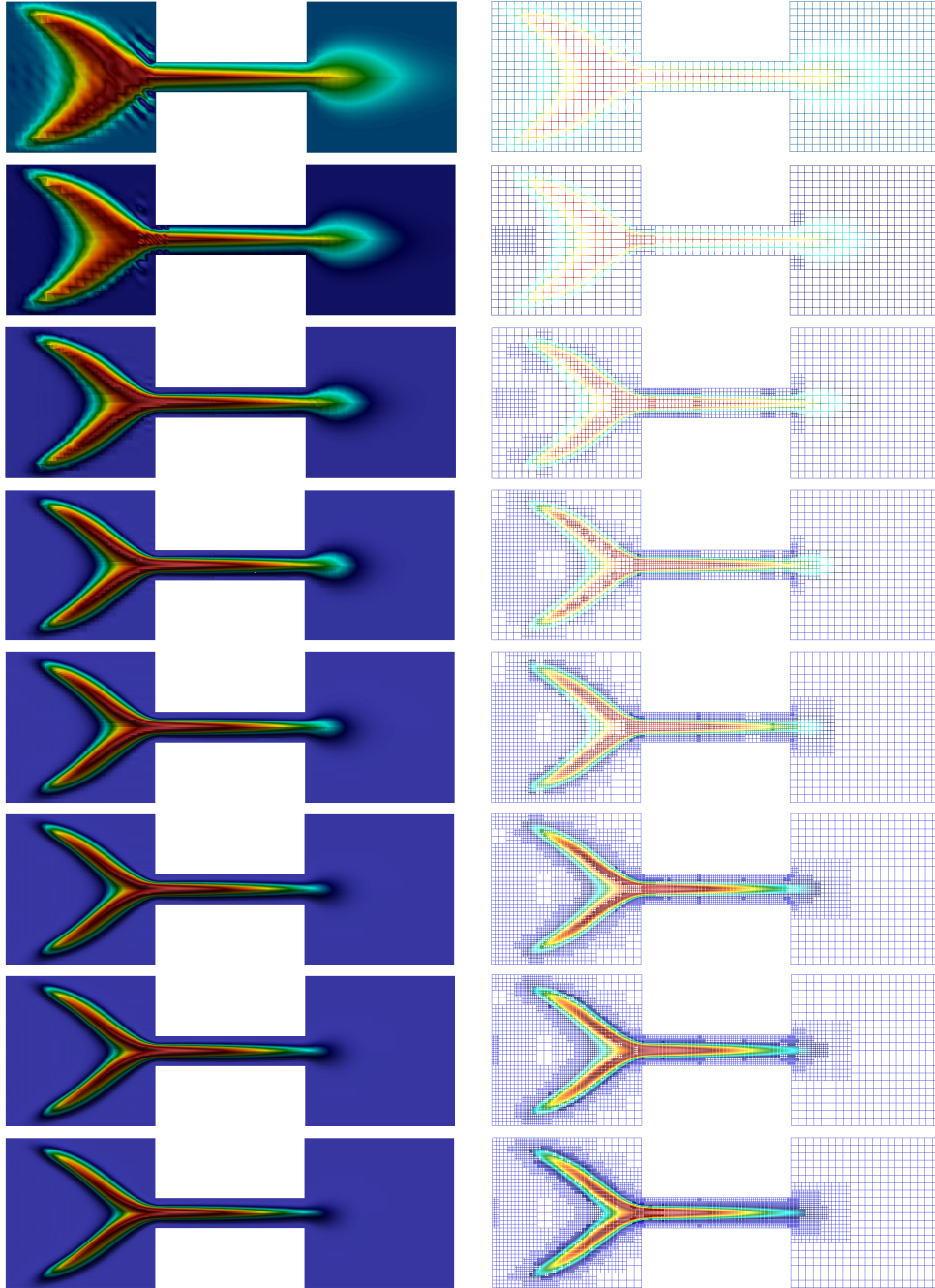


Figure 6.5: Capturing of spurious oscillations with goal-oriented adaptivity illustrated by comparative solution profiles and corresponding meshes of the loops $\ell = 1 - 8$ for Sec. 6.3.

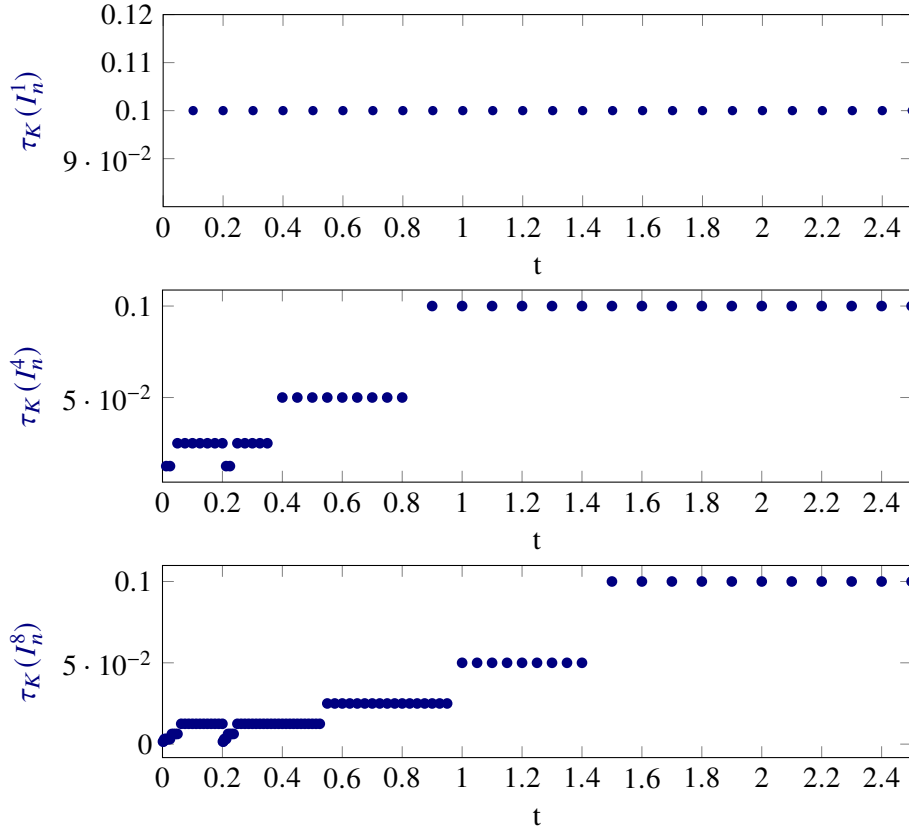


Figure 6.6: Distribution of the temporal step size τ_K of the transport problem for a fixed $\sigma_K = 2.5$ of the Stokes flow problem over the time interval $I = (0, T]$ for the initial (1) and after 4 and 8 DWR-loops.

Finally, we modify the parabolic inflow condition for the Stokes flow problem in order to investigate our multirate-in-time approach for the present example. More precisely, on the left boundary Γ_{inflow} the inflow condition \mathbf{v}_D is now given by

$$\mathbf{v}_D = \begin{cases} \frac{\arctan(t)}{\pi/2} \cdot (1 - 4x_2^2, 0)^\top & \text{for } 0 \leq t \leq 0.1, \\ (1, 0)^\top & \text{for } 0.1 < t \leq T. \end{cases} \quad (6.7)$$

Moreover, for the transport problem, the Dirichlet boundary function value is homogeneous on Γ_D except for the line $(-1, -1) \times (-0.4, 0.4)$ and time $0 \leq t \leq 0.1$ where the constant value

$$u(\mathbf{x}, t) = 1$$

is prescribed on the solution. Therefore, the time domain $I = (0, 2.5)$ is now discretized with the same initial $\tau = \sigma = 0.1$ for the transport and the Stokes flow problem for the first loop $\ell = 1$. In Fig. 6.7 we visualize the distribution of the adaptively determined time cell lengths τ_K and σ_K used for the transport and Stokes flow problem, respectively, over the whole time interval I for different DWR refinement loops. We observe a similar behavior as displayed in Fig. 6.6. The temporal mesh is refined close to the time conditions of the respective inflow boundaries for both problems, where the refinement in time for the Stokes flow problem is chosen to refine those slabs related to the inflow condition (6.7) for each second DWR-loop. Away from the temporal inflow condition both temporal meshes stay coarse.

| ℓ | N | N_K^{\max} | $N_{\text{DoF}}^{\text{tot}}$ | η_h | η_τ |
|--------|-----|--------------|-------------------------------|------------|-------------|
| 1 | 25 | 880 | 24425 | 3.5795e-03 | 1.1452e-02 |
| 2 | 29 | 880 | 28333 | 3.8619e-03 | 3.2318e-03 |
| 3 | 32 | 1456 | 39456 | 2.9354e-03 | 5.4042e-03 |
| 4 | 42 | 2116 | 62528 | 2.5532e-03 | 5.2001e-03 |
| 5 | 51 | 4492 | 132483 | 2.3178e-03 | 5.2170e-03 |
| 6 | 70 | 7072 | 239266 | 1.8934e-03 | 3.8571e-03 |
| 7 | 79 | 10744 | 371015 | 1.7406e-03 | 2.3554e-03 |
| 8 | 89 | 15376 | 619071 | 1.6069e-03 | 1.2974e-03 |

Table 6.5: Goal-oriented temporal and spatial refinements for the transport problem in Sec. 6.3. ℓ denotes the refinement level loop, N the accumulated total cells in time, N_K^{\max} the maximal number of cells on a slab, $N_{\text{DoF}}^{\text{tot}}$ the total space-time degrees of freedom and η_h and η_τ the computed error indicators in space and time, respectively.

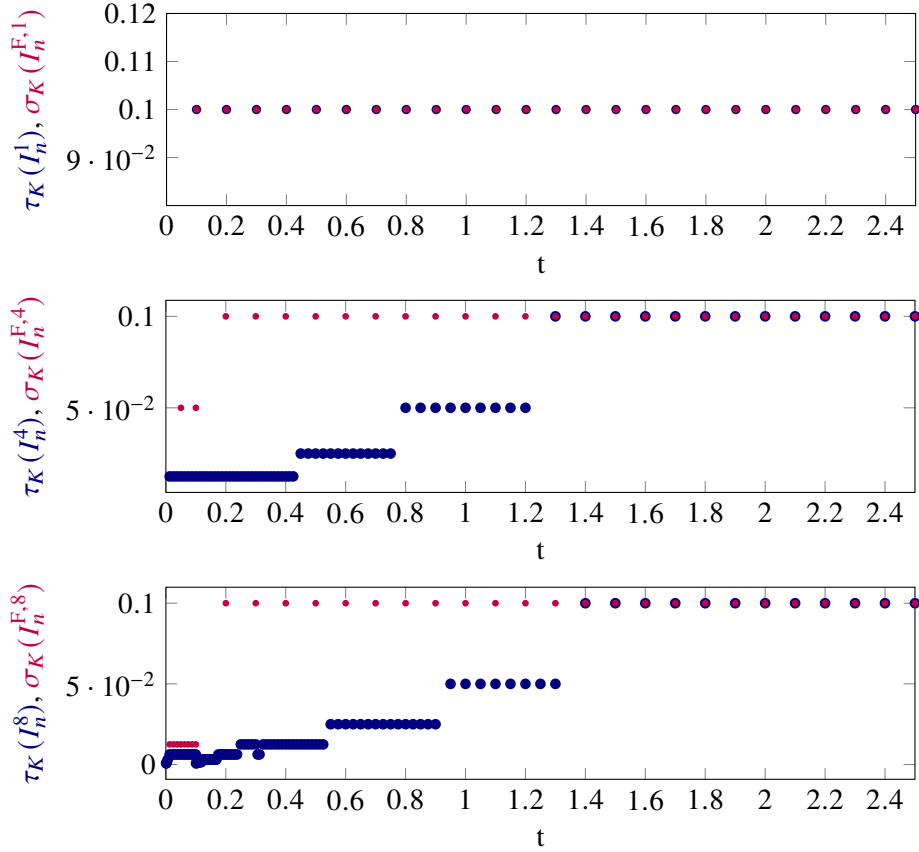


Figure 6.7: Distribution of the temporal step size τ_K of the transport problem and σ_K of the Stokes flow problem over the time interval $I = (0, T]$ for the initial (1) and after 4 and 8 DWR-loops.

7 Conclusion

In this work we presented a multirate-in-time approach regarding different time scales for a rapidly changing transport coupled with a slowly creeping Stokes flow. The transport problem is represented by a convection-dominated convection-diffusion-reaction equation which is for this reason stabilized using the residual based SUPG method. Both subproblems are discretized using a discontinuous Galerkin method dG(r) with an arbitrary polynomial

degree $r \geq 0$ in time and a continuous Galerkin method $cG(p)$ with an arbitrary polynomial degree $p \geq 1$ in space. A goal-oriented a posteriori error representation based on the Dual Weighted Residual method was derived for the transport problem. This error representation is splitted into an amount in space and time whose localized forms serve as error indicators for the adaptive mesh refinement process in space and time. The temporal weights of the DWR adaptivity process are approximated by a higher-order extrapolation approach whereas the spatial weights are approximated by higher-order finite elements. The practical realization of the space-time slabs is based on tensor-product spaces which enables for an efficient and flexible software implementation of the underlying approach. In numerical experiments we verified expected experimental orders of convergence of the underlying subproblems as well as the coupled problem. Furthermore, space-time adaptivity studies for the coupled problem were investigated for an academic test problem as well as a problem of practical interest, leading to high-efficient adaptively refined meshes in space and time. Effectivity indices close to one and well-balanced error indicators in space and time were obtained. Spurious oscillations that typically arise in numerical approximations of convection-dominated problems could be reduced significantly. Finally, the here presented approach for coupled free flow and species transport is fairly general and can be easily adopted to other multi-physics systems coupling phenomena that are characterized by strongly differing time scales.

References

- [1] Jammoul, M., Wheeler, M.F., Wick, T.: A phase-field multirate scheme with stabilized iterative coupling for pressure driven fracture propagation in porous media. *Comput. Math. Appl.* **91**, 176–191 (2021)
- [2] Ge, Z., Ma, M.: Multirate iterative scheme based on mutiphysics discontinuous Galerkin method for a poroelasticity model. *Appl. Numer. Math.* **128**, 125–138 (2018)
- [3] Gupta, S., Wohlmuth, B., Helmig, R.: Multirate time stepping schemes for hydro-geomechanical model for subsurface methane hydrate reservoirs. *Adv. Water Res.* **91**, 78–87 (2016)
- [4] Almani, T., Kumar, K., Dogru, A., Singh, G., Wheeler, M.F.: Convergence analysis of multirate fixed-stress split iterative schemes for coupling flow with geomechanics. *Comput. Meth. Appl. Mech. Engrg.* **311**, 180–207 (2016)
- [5] Gear, C.W., Wells, D.R.: Multirate linear multistep methods. *BIT* **24**(4), 484–502 (1984)
- [6] Günther, M., Rentrop, P.: Multirate ROW methods and latency of electric circuits. *Appl. Numer. Math.* **13**(1), 83–102 (1993)
- [7] Gander, M.J., Halpern, L.: Techniques for locally adaptive time stepping developed over the last two decades. In: Bank, R., Holst, M., Widlund, O., Xu, J. (eds.), *Domain Decomposition Methods in Science and Engineering XX, Lecture Notes in Computational Science and Engineering* **91**, pp. 377–385. Springer, Berlin, Heidelberg (2013)
- [8] Köcher, U., Bruchhäuser, M. P., Bause, M.: Efficient and scalable data structures and algorithms for goal-oriented adaptivity of space–time FEM codes. *Software X*, 10:100239 (2019)
- [9] Arndt, D., Bangerth, W., Blais, B., Fehling, M., Gassmöller, R., Heister, T., Heltai, L., Köcher, U., Kronbichler, M., Maier, M., Munch, P., Pelteret, J.-P., Proell, S., Simon, K.,

- Tureksin, B., Wells, D., Zhang, J.: The deal.II Library, Version 9.3. *J. Numer. Math.* **29**(3), 171–186 (2021)
- [10] Gujer, W.: *Systems Analysis for Water Technology*. Springer, Berlin, Heidelberg (2008)
- [11] Morgenroth, E.: How are characteristic times (τ_{char}) and non-dimensional numbers related.
<https://ethz.ch/content/dam/ethz/special-interest/baug/ifu/water-management-dam/documents/education/Lectures/UWM3/SAMM.HS15.Handout.CharacteristicTimes.pdf>
 (2015). Accessed 07 February 2022
- [12] Burman, E.: Robust error estimates in weak norms for advection dominated transport problems with rough data. *Math. Models Methods Appl. Sci.* **24**(13), 2663–2684 (2014)
- [13] John, V., Knobloch, P., Novo, J.: Finite elements for scalar convection-dominated equations and incompressible flow problems: a never ending story? *Comput. Vis. Sci.* **19**, 47–63 (2018)
- [14] John, V., Schmeyer, E.: Finite element methods for time-dependent convection-diffusion-reaction equations with small diffusion. *Comput. Methods Appl. Mech. Engrg.* **198**, 173–181 (2009)
- [15] Roos, H.-G., Stynes, M., Tobiska, L.: *Robust Numerical Methods for Singularly Perturbed Differential Equations*. Springer, Berlin (2008)
- [16] Becker, R., Rannacher, R.: An optimal control approach to a posteriori error estimation in finite element methods. In: Iserles, A. (Ed.) *Acta Numer.*, Vol. 10, 1–102. Cambridge University Press (2001)
- [17] Bangerth, W., Rannacher, R.: *Adaptive finite element methods for differential equations*. Birkhäuser, Basel (2003)
- [18] Ainsworth, M., Oden, J. T.: *A posteriori error estimation in finite element analysis*. Wiley, New York (2000)
- [19] Verfürth, R.: *A Review of A Posteriori Error Estimation and Adaptive Mesh-Refinement Techniques*. Wiley-Teubner Series Advances in Numerical Mathematics. Wiley-Teubner, New York Stuttgart (1996)
- [20] Bause, M., Bruchhäuser, M.P., Köcher, U.: Flexible goal-oriented adaptivity for higher-order space-time discretizations of transport problems with coupled flow. *Comput. Math. Appl.* **91**, 17–35 (2021)
- [21] Larson, M.G., Målquist, A.: Goal oriented adaptivity for coupled flow and transport with applications in oil reservoir simulations. *Comput. Methods Appl. Mech. Engrg.* **196**, 3546–3561 (2007)
- [22] Allaire, G.: Homogenization of the Stokes flow in a connected porous medium. *Asymptotic Anal.* **2**, 203–222, (1989)
- [23] Wick, T.: Goal functional evaluations for phase-field fracture using PU-based DWR mesh adaptivity. *Comput. Mech.* **57**, 1017–1035 (2016)
- [24] Odsäter, L.H., Kvamsdal, T., Larson, M.G.: A simple embedded discrete fracture-matrix model for a coupled flow and transport problem in porous media. *Comp. Methods Appl. Mech. Engrg.* **343**, 572–601 (2019)

- [25] Bengzon, F., Larson, M. G.: Adaptive finite element approximation of multiphysics problems: a fluid-structure interaction model problem. *Int. J. Numer. Methods Eng.* **84**, 1451–1465 (2010)
- [26] John, V.: Finite element methods for incompressible flow problems. Springer Series in Computational Mathematics, Vol. 51, Springer, Cham (2016)
- [27] Ern, A., Guermond, J.-L.: Finite elements III: First-order and time-dependent pdes. vol. 74, Texts in Applied Mathematics, Springer, Cham (2021)
- [28] Carey, G. F., Oden, J. T.: Finite Elements, Computational Aspects, Vol. III (The Texas finite element series). Prentice-Hall, Englewood Cliffs, New Jersey (1984)
- [29] Hughes, T. J. R., Brooks, A. N.: A multidimensional upwind scheme with no crosswind diffusion. In: Hughes, T. J. R. (Ed.) *Finite Element Methods for Convection Dominated Flows*, AMD, Vol. 34, pp. 19–35. Amer. Soc. Mech. Engrs. (ASME) (1979)
- [30] Brooks, A. N., Hughes, T. J. R.: Streamline upwind/Petrov-Galerkin formulations for convection dominated flows with particular emphasis on the incompressible Navier-Stokes equations. *Comput. Methods Appl. Mech. Engrg.* **32**(1-3), 199–259 (1982)
- [31] John, V., Novo, J.: Error analysis of the SUPG finite element discretization of evolutionary convection-diffusion-reaction equations. *SIAM J. Numer. Anal.* **49**(3), 1149–1176 (2011)
- [32] Besier, M., Rannacher, R.: Goal-oriented space-time adaptivity in the finite element galerkin method for the computation of nonstationary incompressible flow. *Int. J. Num. Methods Fluids* **70**(9), 1139–1166 (2012)
- [33] Bruchhäuser, M. P., Schwegler, K., Bause, M.: Dual weighted residual based error control for nonstationary convection-dominated equations: potential or ballast?. In: Barrenechea G. R., Mackenzie, J. (Eds.), *Boundary and Interior Layers, Computational and Asymptotic Methods BAIL 2018*, Lecture Notes in Computational Science and Engineering **135**, Springer, Cham, 1–17 (2020)